Comparative Brain-Wide Mapping of Isoflurane and Ketamine-Activated Nuclei and Functional Networks

Yue Hu[1†], **Jiangtao Qi**[1†], **Zhao Zhang**[1], **Mengqiang luo**[1*], **Yingwei Wang**[1*]

[1]Department of Anesthesiology, Huashan Hospital, Fudan University, 12 Middle Wulumuqi Road, Shanghai 200040, China

***For correspondence:**
luomq16@fudan.edu.cn (FS);
wangyw@fudan.edu.cn (FMS)

[†]These authors contributed equally to this work

Abstract Ketamine (KET) and isoflurane (ISO) are two widely used general anesthetics, yet their distinct and shared neurophysiological mechanisms remain elusive. In this study, we conducted a comparative analysis of KET and ISO effects on c-Fos expression across the brain, utilizing hierarchical clustering and c-Fos-based functional network analysis to evaluate the responses of individual brain regions to each anesthetic. Our findings demonstrate that KET significantly activates cortical and subcortical arousal-promoting nuclei, with the temporal association areas (TEa) serving as a hub node, corroborating the top-down general anesthesia theory for dissociative anesthesia. In contrast, ISO activates the nuclei in the hypothalamus and brainstem, with the locus coeruleus (LC) as a hub node, implying a bottom-up mechanism for anesthetic-induced unconsciousness. Notably, the coactivation of arousal-related nuclei, analgesia-related, neuroendocrine-related nuclei (e.g., prelimbic area (PL) and infralimbic areas (ILA), and the anterior paraventricular nucleus (aPVT), Edinger-Westphal nucleus (EW), locus coeruleus (LC), parabrachial nucleus (PB), solitary tract nucleus (NTS) by both anesthetics underscores shared features such as unconsciousness, analgesia, and autonomic regulation, irrespective of their specific molecular targets. In conclusion, our results emphasize the distinct actions of KET and ISO while also uncovering the commonly activated brain regions, thus contributing to the advancement of our understanding of the mechanisms underlying general anesthesia.

Introduction

Despite considerable investigation into the molecular targets, neural circuits, and functional connectivity associated with various anesthetics, our comprehension of their effects on overall brain activity continues to be limited and incomplete (***Hemmings et al., 2019***). At the molecular level, ketamine (KET) and isoflurane (ISO) interact with N-methyl-D-aspartate (NMDA) and gamma-aminobutyric acid type A (GABAa) receptors, respectively, modulating neuronal excitability and ultimately leading to a loss of consciousness (***Franks, 2008***). In systems neuroscience, the neural mechanisms of anesthetic induced unconsciousness involve both top-down and bottom-up processes (***Mashour, 2014***; ***Mashour and Hudetz, 2017***). As evidenced by in vivo electrophysiology or functional magnetic resonance imaging (fMRI) studies, the top-down paradigm illustrates that anesthetics induce unconsciousness by disrupting corticocortical and corticothalamic circuits responsible for neural information integration, while peripheral sensory information can still be conveyed to the primary sensory cortex (***Schroeder et al., 2016***; ***Lee et al., 2013***). The bottom-up approach, exemplified by ISO, involves the activation of sleep-promoting nuclei like ventral lateral preoptic nucleus (VLPO)

and inhibition of arousal centers in the brainstem and diencephalon, supporting the shared circuits of sleep and anesthesia (***Moore et al., 2012***; ***Nelson et al., 2002***). However, the limited spatial resolution of fMRI studies and the inability of EEG to capture specific brainstem nuclei hinder the acquisition of comprehensive whole-brain information. Although a substantial body of knowledge has been amassed, our understanding of the reciprocal responses among different brain regions during general anesthesia remains relatively sparse and fragmented. To bridge these gaps, further investigation using advanced techniques that can capture the whole-brain dynamics is needed to elucidate the complex interactions and shared mechanisms between various anesthetics.

Neuronal extracellular stimulation typically results in the elevation of adenosine 3',5'-cyclic monophosphate (cAMP) levels and calcium influx, ultimately leading to the upregulation of immediate early genes (IEGs) such as c-fos (***Yap and Greenberg, 2018***; ***Morgan and Curran, 1989***). The translation product of c-fos, c-Fos protein, offers single-cell spatial resolution and has been utilized as a biomarker to identify anesthetic-activated brain regions (***Zhang et al., 2022***). Previous investigations of c-Fos expression throughout the brain demonstrated that GABAergic agents inhibited cortical activity while concurrently activating subcortical brain regions, including the VLPO, median preoptic nucleus (MnPO), lateral septal nucleus (LS), Edinger-Westphal nucleus (EW), and locus coeruleus (LC) (***Smith et al., 2016***; ***Lu et al., 2008***; ***Yatziv et al., 2020***; ***Han et al., 2014***). In contrast, KET was shown to provoke wake-like c-Fos expression and intense augmentation of c-Fos expression in various brain regions at clinical dosages (75-100 mg/kg) (***Lu et al., 2008***). It is important to note that these experiments administered KET at lights-on and GABAa receptor agonists at lights-off, potentially introducing circadian influences for direct comparison of ISO and KET. Moreover, it has been revealed that state of general anesthesia is not determined by activity in individual brain areas, but emerges as a global change within the brain. This change involves the activation of lateral habenular nucleus (LHb), VLPO, supraoptic nucleus (SO), and central amygdaloid nucleus (CeA), which are essential for anesthetics induced sedation, unconsciousness, or analgesia (***Moore et al., 2012***; ***Gelegen et al., 2018***; ***Hua et al., 2020***; ***Jiang-Xie et al., 2019***). However, brain-wide mapping and comparison of distinct anesthetic (KET and ISO) activated nuclei at a cellular level have not been fully elucidated.

In this study, we examined the distribution of nuclei activated by ISO and KET in 984 brain regions using immunochemical labeling and a customized MATLAB software package, which facilitated signal detection and registration to the Allen Mouse Brain Atlas reference (***Ma et al., 2021***). We compared whole-brain c-Fos expression induced by KET and ISO through hierarchical clustering and calculated inter-regional correlations by determining the covariance across subjects for each brain region pair. Significantly positively correlated regions were then extracted to construct functional networks and graph theory-based analyses were performed to identify hub nodes. Our results revealed distinct yet overlapping whole-brain activation patterns for KET and ISO.

Results

A comparison of the activation patterns of c-Fos in 53 brain areas in response to ISO and KET

To examine the pattern of c-Fos expression throughout the brain, 1.5% ISO was continuously ventilated, or 100 mg/kg KET was administered 90 minutes before harvesting (Figure 1A). Sample collection for all mice was uniformly conducted at 14:30 (ZT7.5), and the c-Fos labeling and imaging were performed using consistent parameters throughout all experiments. To quantitatively assess brain states across the four groups, we utilized electroencephalography (EEG) and electromyography (EMG) recordings (Figure 1—figure supplement 1). The depth of anesthesia was evaluated based on the power ratio of the EEG within the delta (0.5–4 Hz) and theta (6–10 Hz) frequency bands, combined with the changes in the EMG (***Luo et al., 2023***). Our findings showed that ISO and KET elevated EEG power ratio while reducing EMG power, suggesting both drugs induced a loss of consciousness. The raw images of brain slices were aligned to the Allen Mouse Brain Atlas (Figure

1B). Based on the standard mouse atlas available at http://atlas.brain-map.org/, the mouse brain was segmented into nine hierarchical levels, totaling 984 regions. The primary level consists of grey matter, the secondary of the cerebrum, brainstem, and cerebellum, and the tertiary includes regions like the cerebral cortex and cerebellar nuclei, among others, with some regions extending to the 8th and 9th levels. The fifth level comprises 53 subregions, with detailed expression levels and their respective abbreviations presented in Figure 2—figure supplement (***Do et al., 2016***).

To determine the effects of ISO and KET on neural activity, we normalized c-Fos densities across brain regions to their control group averages region by region and log-transformed the data. Hierarchical clustering of these values revealed distinct patterns of drug-induced changes (Figure 2A), with both ISO and KET showing optimal clustering at a 0.5 cut-off value, as confirmed by high silhouette coefficients (Figure 2B). Concurrently, we computed the number of clusters formed at each potential cut-off value and found that a 0.5 threshold resulted in four distinct clusters for both ISO and KET treatments (Figure 2C). After hierarchical clustering, we maintained the sequence of brain regions and substituted log relative c-Fos densities with Z-scores for both ISO and KET (Figure 2E). While no significantly inhibited brain regions were detected in the ISO group (as no Z scores fell below -2), clusters 3 and 4 showed expression levels similar to or lower than those in the control group. These clusters are involved in sensory integration, motor coordination, and higher-order cognitive processing, with cluster 3 having a mean Z score of 0.27 (n=17) and cluster 4 a mean Z score of -1.1 (n=2), as shown in Figures 2D and 2E. The most pronounced upregulation of ISO induced c-Fos expression was observed in the second cluster (n=13, mean Z score=4.7), which includes brain regions responsible for a variety of functions: the periventricular zone (PVZ) and lateral zone (LZ) of the hypothalamus, vital for endocrine and autonomic system regulation; the ventral striatum (STRv), pallidum (PAL), and lateral septal complex (LSX) of the striatum, key in reward and motivation; the tenia tecta (TT) and piriform area (PIR), essential for olfactory processing; and the infralimbic area (ILA) of the cortex, significant for emotional and cognitive functions. This collective upregulation in cluster 2 underlines ISO's impact on hypothalamic regulation, reward mechanisms, and olfactory processing. KET administration elicited a significant activation in a broad array of brain regions, with Cluster 4 displaying the most substantial upregulation in expression. This cluster incorporates cortical areas central to sensory processing and emotional regulation, such as the visceral area (VISC), anterior cingulate area (ACA), and primary somatosensory cortex (SS) — as well as cerebral nuclei integral for motor coordination and motivational behaviors — specifically, the dorsolateral and ventrolateral pallidum (PALd, PALv) and striatum (STRd, STRv) (Figures 2D and 2E). ISO predominantly modulates brain regions associated with hormonal regulation, reward processing, and olfaction, with marked activation in the hypothalamic and striatal regions. In contrast, KET induces widespread activation across the brain, with heightened activity in a key cluster that includes cortical and cerebral nuclei governing complex sensory, emotional, and motor processes, thus highlighting its notable influence on higher-order functions.

Similarities and differences in ISO and KET activated c-Fos brain areas

To enhance our analysis of c-Fos expression patterns induced by ISO and KET, we expanded our study to 201 subregions. After log-transforming the c-Fos densities relative to controls, we applied hierarchical clustering to uncover patterns of brain activity (Figure 3A), with detailed expression levels in Figure 3—figure supplement 1. ISO demonstrates a more concentrated influence on brain activity with consistently higher clustering quality and fewer clusters than KET, suggesting a focused impact on specific brain functions (Figures 3B and 3C). Figure 3E maintains the order from hierarchical clustering and marks both the most activated brain regions in the top 10% of Z-scores with red boxes and areas of potential suppression with Z-scores below -2 with white boxes. ISO hierarchical clustering identified three distinct clusters, with cluster 3 exhibiting the highest mean Z-score of 7.27. This cluster encompasses regions like the supraoptic (SO), ventrolateral preoptic (VLPO), tuberal (TU), and central amygdala (CEA). Notably, the SO, VLPO, and CEA have been previously reported to play critical roles in the mechanisms of anesthesia (***Moore et al., 2012***; ***Hua et al.,***

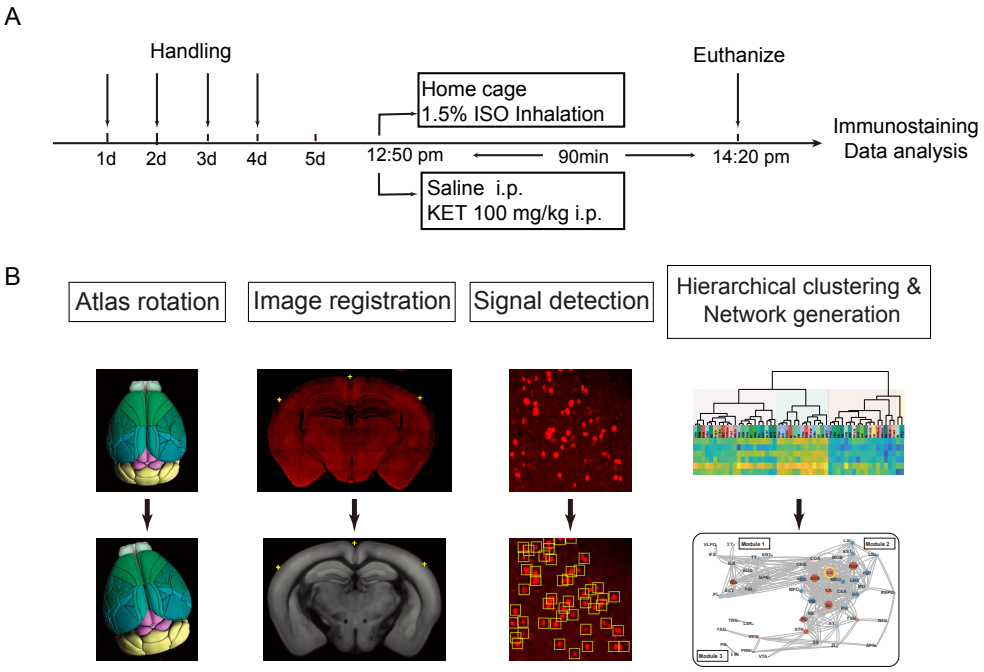

Figure 1. Brain-wide quantification of c-Fos expression. (A)Schematic representation of the habituation protocol typically used to acclimate mice. After being exposed to anesthetics for 90 minutes, the mice were euthanized. (B) Steps for data processing. Example of brain section registration to a corresponding coronal section from the Allen Brain Atlas. For Atlas rotation, the Allen reference atlas was rotated to mimic the slice angle of the experimental brain. Image registration maps the original coronal image (upper panel) to the corresponding Allen mouse brain atlas (lower panel). The registration module applies several geometric transformations (translation, rotation, and scaling) to optimize the matching of the original image to the anatomical structures. Fluorescence signals detected in the original image were projected onto the Allen Mouse Brain Atlas for quantification. Finally, the processed data undergo hierarchical clustering and network analysis to investigate the patterns of c-Fos expression and central network nodes.

Figure 1—figure supplement 1. EEG and EMG power change after each treatment. The box represents the 25th-75th percentiles; the central line denotes the median; whiskers indicate maximum and minimum values. n = 6, 6, 8, 6 for the home cage, ISO, saline, and KET, respectively. (A) Normalized change in EEG power: ISO vs KET, P > 0.99; Saline vs KET, P = 0.01; Home cage vs ISO, P = 0.11. (B) Normalized change in EMG power: ISO vs KET, P = 0.36; Saline vs KET, P = 0.30; Home cage vs ISO, P = 0.02. Analyses were conducted using the Kruskal-Wallis test, followed by Dunn's multiple comparisons tests.

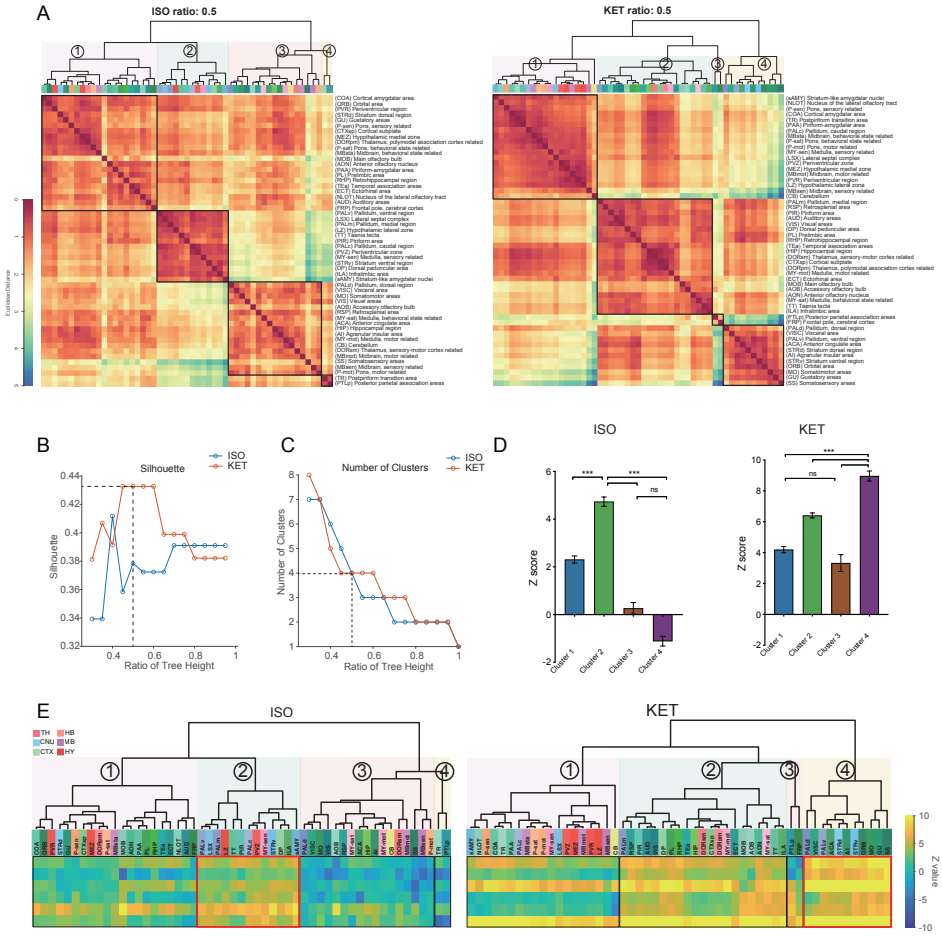

Figure 2. Whole-brain distributions of c-Fos+ cells induced by ISO and KET. (A) Hierarchical clustering was performed on the log relative c-Fos density data for ISO and KET using the complete linkage method based on the Euclidean distance matrix, with clusters identified by a dendrogram cut-off ratio of 0.5. Numerical labels correspond to distinct clusters within the dendrogram. (B) Silhouette values plotted against the ratio of tree height for ISO and KET, indicating relatively higher Silhouette values at 0.5 (dashed line), which is associated with optimal clustering. (C) The number of clusters identified in each treatment condition at different ratios of the dendrogram tree height, with a cut-off level of 0.5 corresponding to 4 clusters for both ISO and KET (indicated by the dashed line). (D) The bar graph depicts Z scores for clusters in ISO and KET conditions, represented with mean values and standard errors. One-way ANOVA with Tukey's post hoc multiple comparisons. ns: no significance; ***P < 0.001. (E) Z-scored log relative density of c-Fos expression in the clustered brain regions. The order and abbreviations of the brain regions and the numerical labels correspond to those in Figure 2A. The red box denotes the cluster with the highest mean Z score in comparison to other clusters. CTX: cortex; TH: thalamus; HY: hypothalamus; MB: midbrain; HB: hindbrain.

Figure 2—figure supplement 1. The c-Fos density in 53 brain areas for different conditions. (home cage, n = 6; ISO, n = 6 mice; saline, n = 8; KET, n = 6). Each point represents the c-Fos density in a specific brain region, denoted on the y-axis with both abbreviations and full names. Data are shown as mean ± SEM. Brain regions are categorized into 12 brain structures, as indicated on the right side of the graph.

2020; ***Jiang-Xie et al., 2019***). In contrast, cluster 1 showed a relative decrease in expression (n= 91, mean Z-score: -0.54), indicating that nearly half of the brain areas had reduced c-Fos expression compared to the control group. Cluster 2 was overall moderately activated, with significant activity in the top 10% of regions including the anterior hypothalamic (ARH) and paraventricular (PVH) nuclei—key for hypothalamic functions—and cortical areas such as the infralimbic (ILA), dorsal peduncular (DP), and temporal (TT) cortices, which are involved in emotional and cognitive processing. Striatal and pallidal regions, particularly the olfactory tubercle (OT) and nucleus accumbens (ACB), as well as midbrain and hindbrain structures like the area postrema (AP) and nucleus of the solitary tract (NTS), showed the most pronounced activation. In the hierarchical clustering analysis of KET exposure, Cluster 2 with a mean Z-score of -0.01 was similar to the control group in terms of activation, while the other four clusters showed increased activation. Cluster 5, showing the most significant activation, is composed mainly of cortical regions critical for sensory processing, spatial memory, navigation, emotional regulation, and cognitive functions. It also includes cerebral nuclei involved in motor control and reward pathways, alongside essential thalamic and hindbrain areas for memory and sensory transmission. This composition, with a predominant focus on cortical regions, suggests that KET chiefly modulates higher-order brain functions, while also affecting basic neurological processes through its influence on cerebral nuclei, the thalamus, and the hindbrain. In conclusion, while ISO's activation of specific areas like SO, VLPO, TU, and CeA in cluster 3 indicates a targeted influence, KET's extensive engagement with cortical areas in cluster 5, along with its effects on striatal and thalamic regions, underscores its profound and widespread modulation of both higher-order and fundamental neural functions.

Identification of brain regions activated by KET

We further employed quantitative methods to identify the brain regions activated by KET across the entire brain. Our findings concur with previous studies: numerous cortical regions associated with somatosensory, auditory, visual, and movement were activated (Figure 4A and C, Figure 4—figure supplement 1, Figure 4—source data 1). Additionally, we identified several innovative observations that enrich the current understanding in this field. To provide a clearer overview of our findings, we categorized the activated brain areas into different functional groups: (1) Arousal and REM sleep regulation: Several nuclei associated with arousal were activated, including the prelimbic area (PL), infralimbic cortex (ILA), paraventricular nucleus of the thalamus (PVT), dorsal raphe (DR), and sublaterodorsal nucleus (SLD). Prior evidence indicates that the PL/ILA and PVT regions play a role in regulating arousal in both cortical and subcortical areas (***Mashour et al., 2022***; ***Gao et al., 2020***). Additionally, dopaminergic neurons within the DR have been identified as vital components of wake-promoting pathways (***Cho et al., 2017***). In the context of REM sleep, the sublaterodorsal nucleus (SLD) stands out for its role in stabilization (***Feng et al., 2020***). (2) Pain modulation: KET significantly activated pain-related areas such as the anterior cingulate cortex (ACA) in the cortex (***Bliss et al., 2016***), the anterior pretectal nucleus (APN) in the thalamus, which is known to be involved in managing chronic pain (***Villarreal et al., 2003***), and the anterior periaqueductal gray (PAG) region and medial prefrontal cortex (mPFC), both part of the endogenous pain inhibitory pathway (***Cheriyan and Sheets, 2018***; ***Yeung et al., 1977***). Additionally, the activation of the locus coeruleus (LC) in the midbrain may contribute to KET's analgesic effects (***Llorca-Torralba et al., 2021***). (3) Neuroendocrine regulation: The paraventricular hypothalamic nucleus (PVH) and supraoptic nucleus (SO), which are neuroendocrine-related regions, were also activated (***Jiang-Xie et al., 2019***; ***Duncan et al., 1998***). (4) Movement: Subcortical nuclei associated with movement, such as the subthalamic nucleus (STN) and nucleus incertus (NI), were prominently activated by KET administration (***Ma et al., 2017***; ***Musacchio et al., 2017***). (5) Connectivity: We observed significant activation of the nucleus reuniens (Re) located in the thalamus, which receives substantial afferent input from limbic structures and serves as a connector linking the hippocampus to the medial prefrontal cortex (***Hauer et al., 2021***). While our functional categorization offers a simplified overview, it's worth noting that each activated brain region may have multifaceted roles beyond this classification. In

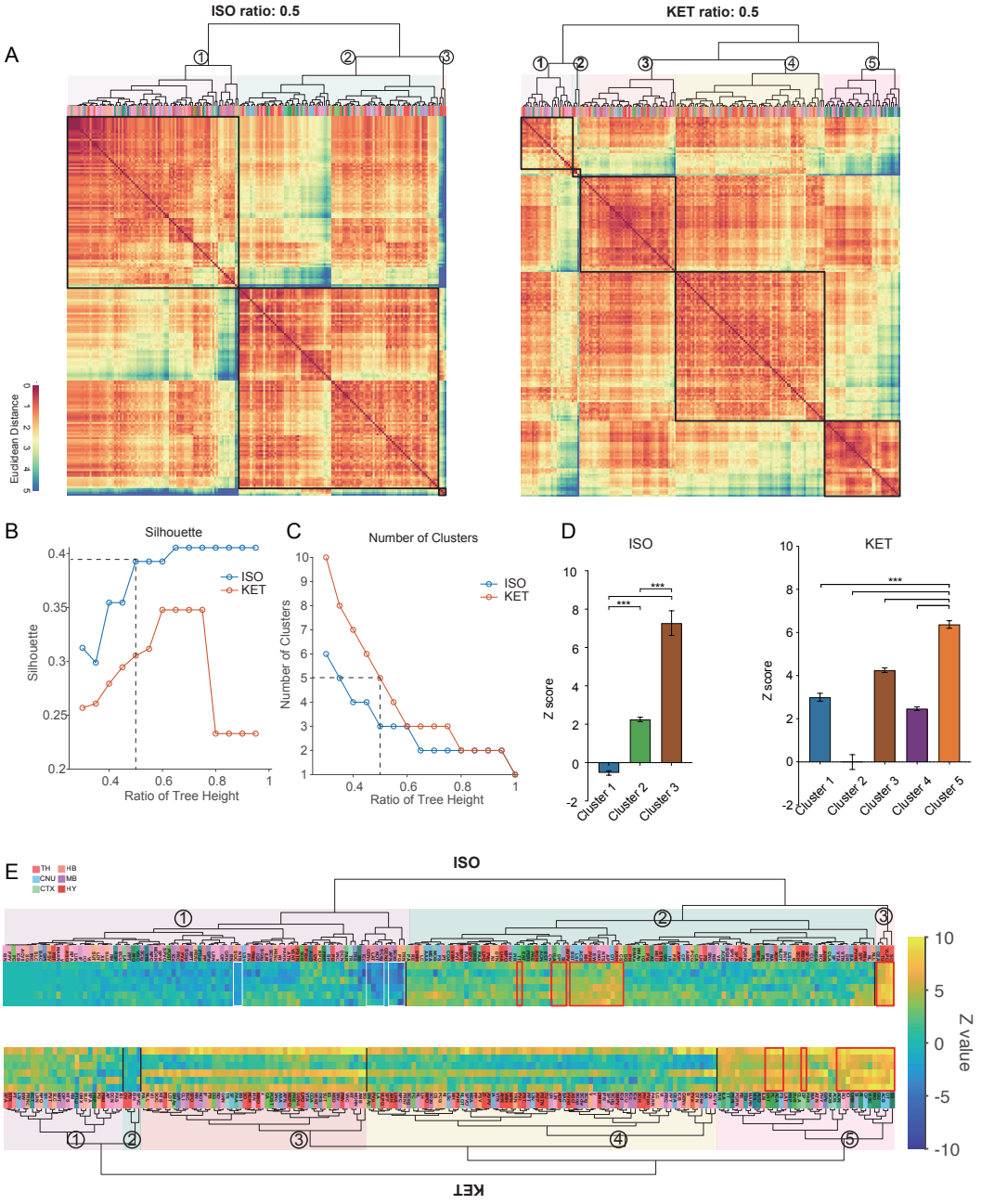

Figure 3. Similarities and differences in ISO and KET activated c-Fos brain areas. (A) Hierarchical clustering was performed on the log-transformed relative c-Fos density data for ISO and KET using the complete linkage method based on the Euclidean distance matrix, with clusters identified by a dendrogram cut-off ratio of 0.5. Brain region labels are provided in Supplementary Figures 4 and 5. (B) Silhouette values are plotted against the ratio of tree height from the hierarchical clustered dendrogram in Figure 3A. (C) The relationship between the number of clusters and the tree height ratio of the dendrogram for ISO and KET, with a cut-off ratio of 0.5 resulting in 3 clusters for ISO and 5 for KET (indicated by the dashed line). (D) The bar graph depicts Z scores for clusters in ISO and KET conditions, represented with mean values and standard errors. One-way ANOVA with Tukey's post hoc multiple comparisons. ns: no significance; ***P < 0.001. (E) Z-scored log relative density of c-Fos expression within the identified brain region clusters. The arrangement, abbreviations of the brain regions, and the numerical labels are in accordance with Figure 3A. The red boxes highlight brain regions that rank within the top 10 percent of Z score values. The white boxes denote brain regions with an Z score less than -2.

Figure 3—figure supplement 1. c-Fos density visualization across 201 distinct brain regions under various conditions. The graph depicts the c-Fos density levels for each condition, with data presented as mean and standard error. Brain regions with statistically significant differences are featured in Figures 4 and 5. Brain regions are organized into major anatomical subdivisions, as indicated on the left side of the graph.

Figure 3—figure supplement 2. Region labels for the hierarchical clustering of the ISO group in Figure 3A.

Figure 3—figure supplement 3. Region labels for the hierarchical clustering of the KET group in Figure 3A.

summary, our study identified extensive activation of cortical and subcortical nuclei during KET anesthesia, encompassing regions related to arousal, pain modulation, neuroendocrine regulation, movement, and connectivity.

Identification of brain regions activated by ISO

To identify brain regions activated by ISO and compare these with those activated by KET. We began by summarizing previously reported ISO activated nuclei, including PIR, LSd/LSv, CeA in the cortex and striatum, and VLPO, MnPO, EW, NTS, LC, ventral group of the dorsal thalamus (VeN), and area postrema (AP) in the hypothalamus and midbrain (Figure 5—source data 1). We subsequently conducted a comprehensive MATLAB-based analysis of c-Fos expression throughout the entire brain, uncovering previously undetected activated nuclei (Figure 5A, Figure 5—figure supplement 1). Newly identified activated nuclei in the CTX and the CNU included PL/ILA and ENT, aPVT in the thalamus, TU, ARH, PVi, and PVH in the hypothalamus, and PB in the hindbrain. All nuclei activated by ISO in this study were functionally classified and depicted in Figure 5C. Our results confirmed the activation of several brain regions involved in arousal-related nuclei, such as the prelimbic area (PL) and infralimbic areas (ILA), and the paraventricular nucleus (PVT) (***Mashour et al., 2022***; ***Gao et al., 2020***). Additionally, we observed activation in previously reported analgesia-related nuclei, including CeA and LC, as well as the parabrachial nucleus (PB) (***Jiang-Xie et al., 2019***; ***Llorca-Torralba et al., 2021***; ***Deng et al., 2020***). We also found activation in neuroendocrine function-related nuclei of the hypothalamus, such as TU, PVi, ARH, PVH, and SO. Moreover, we identified activations related to ISO induced side effects, such as in the piriform cortex (PIR) and ENT (***Bekkers and Suzuki, 2013***; ***Xu and Wilson, 2012***), which may be stimulated by ISO odor, and the solitary tract nucleus (NTS), potentially responsible for ISO induced vomiting (***Gupta et al., 2017***). The only activated nucleus in the midbrain was the Edinger-Westphal nucleus (EW). Recent research has found that sevoflurane activates EW and is involved in sleep induction and maintenance of anesthesia, suggesting its crucial role in general anesthesia (***Yi et al., 2023***). By comparing the ISO and KET induced c-Fos expression, we summarized the brain regions activated by both anesthetics in Figure 5D. Despite variations in molecular targets, the coactivation of regions such as PL/ILA, aPVT, CeA, PVH, SO, EW, PB, LC, and NTS by both ISO and KET suggests an overlapping neuronal circuitry that influences sleep-wake regulation, analgesia, and neuroendocrine functions. This shared neural circuitry may potentially offer a common mechanism across the two anesthetics for the maintenance of general anesthesia.

Network generation and Hub identification

Previous research has established that general anesthesia is mediated by various brain regions (***Moore et al., 2012***; ***Gelegen et al., 2018***; ***Hua et al., 2020***; ***Jiang-Xie et al., 2019***). C-Fos expression serves as an indicator of neuronal activity, providing a single index of activation per region per animal. By examining the covariance of c-Fos expression across animals within each group, we can infer interactions between brain regions and identify functional networks engaged during general anesthesia (***Wheeler et al., 2013***). We initially incorporated a total of 63 brain regions, including nuclei that were significantly activated by ISO and KET (as indicated by positive findings in Figures 4 and 5) and those previously reported to be associated with the mechanisms of general anesthesia and sleep-wakefulness (***Leung et al., 2014***). We first calculated a comprehensive set of interregional correlations for four groups (Figure 6A). Correlation analysis revealed similar network connectivity and densities between the ISO and home cage groups (mean interregional correlations: Fisher Z = -0.018, P = 0.98; network densities: 0.10 vs. 0.09). In contrast, KET significantly increased network density (0.46 vs. 0.06) and mean interregional correlations compared to the saline group (Fisher Z = 3.54, P < 0.001; Figure 6—figure supplement 1D), indicating enhanced interregional correlation with KET administration. Additionally, we segmented the functional network into modules based on the hierarchical clustering of correlation coefficients (Figure 6—figure supplement 1A). We chose to cut the tree at a value of 0.7 for the relatively high value of Silhouette

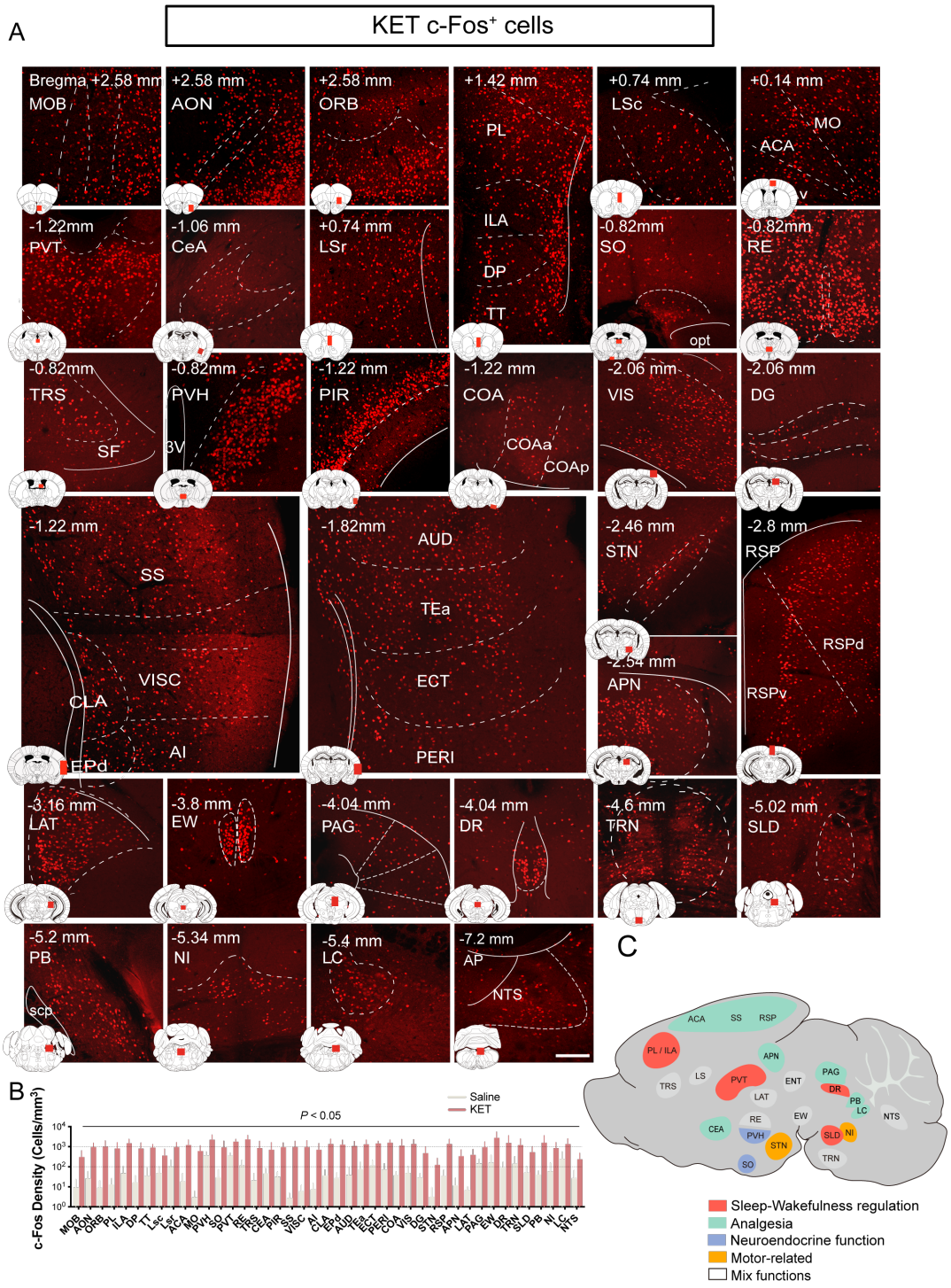

Figure 4. c-Fos expression in distinct brain regions after exposure to KET. (A) Representative immunohistochemical staining of MOB, AON, ORB, MPO, ACA, MO, TRS, PL, ILA, DP, LS, PVT, SO, PVH, RE, VISC, AI, CLA, EPd, PIR, COA, AUD, TEa, ECT, PERI, CeA, SS, DG, STN, RSP, APN, LAT, EW, DR, PAG, SLD, PB, TRN, NI, LC, NTS, and NI c-Fos+ cells from the indicated mice. Scale bar, 200 μm. (B) Representation of c-Fos density in brain regions exhibiting significant statistical differences. Data are shown as mean ± SEM. P values < 0.05. (C) Schematic cross-section of the mouse brain showing activated brain regions by KET. Different colors indicate distinct functional nuclei. The red nuclei are associated with the regulation of sleep-wakefulness, the blue-green nuclei are linked to analgesia, the yellow nuclei are associated with motor function, and the white nuclei are a composite of various functional nuclei.

Figure 4—figure supplement 1. c-Fos expression in specific brain regions following normal saline administration. (A) Representative immunohistochemical staining of c-Fos+ cells in MOB, AON, ORB, MPO, ACA, MO, TRS, PL, ILA, DP, LS, PVT, SO, PVH, RE, VISC, AI, CLA, EPd, PIR, COA, AUD, TEa, ECT, PERI, CeA, SS, DG, STN, RSP, APN, LAT, EW, DR, PAG, SLD, PB, TRN, NI, LC, and NTS. Scale bar represents 200 μm.

Table 1. Figure 4—source data 1. Summary of prior studies on ketamine activated brain regions identified via c-Fos immunostaining.

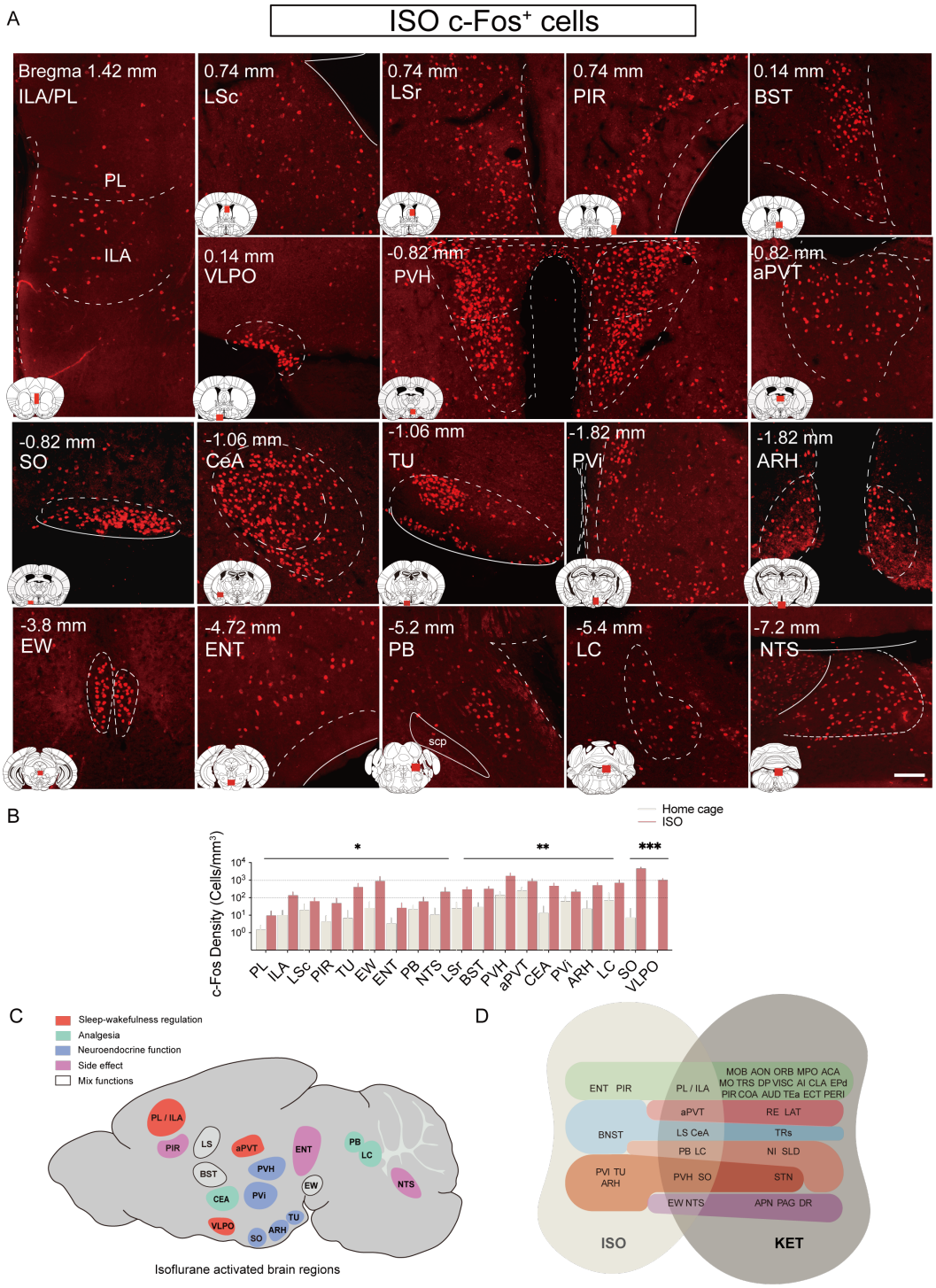

Figure 5. c-Fos expression in distinct brain regions after exposure to ISO. (A) Representative of brain regions with statistical differences c-Fos+ cells between the ISO group and home cage mice. Scale bar, 200 μm. (B) Representation of cell counts in brain regions exhibiting significant statistical differences between home cage and ISO. Data are shown as mean ± SEM. *P<0.05, **P<0.01, ***P<0.001. (C) Schematic cross-section of the mouse brain showing activated brain regions by ISO. Different colors indicate various functionally relevant nuclei. Red signifies nuclei involved in sleep-wake regulation, blue-green in pain management, blue in neuroendocrine function, pink in side-effect management, and white denotes nuclei exhibiting mixed functionalities. (D) The Venn diagram shows brain regions that are co-activated by ISO and KET and differentially activated brain regions.

Figure 5—figure supplement 1. c-Fos expression in home cage group. (A) Representative immunohistochemical staining of c-Fos+ cells in PL, ILA, LSc, LSr, PIR, BST, VLPO, PVH, aPVT, SO, CeA, TU, PVi, ARH, EW, ENT, PB, LC, and NTS c-Fos+ cells from the indicated mice. Scale bar, 200 μm.

Table 2. Figure 5—source data 1. Summary of prior studies on brain regions activated by isoflurane, as detected through c-Fos immunostaining.

scores, resulting in two modules for the home cage and KET groups, and four for the saline and ISO groups (Figure 6—figure supplement 1B and C). Networks were formed using Pearson's coefficients over 0.82 and significant correlations ($P < 0.05$), leaving a single module for KET and three modules for ISO (Figure 6B).

Hubs are nodes that occupy critical central positions within the network, enabling the network to function properly. Due to the singular module structure of the KET network and the sparsity of intermodular connections in the home cage and saline networks, the assessment of network hub nodes did not employ within-module degree Z-score and participation coefficients, as these measures predominantly underscore the importance of connections within and between modules (***Kimbrough et al., 2020***). The analysis evaluated nodal importance using degree (number of direct connections), betweenness centrality (proportion of shortest network paths passing through a node), and eigenvector centrality (influence based on the centrality of connected nodes), identifying brain regions that scored highly in all three as hub nodes (Figure 6—figure supplement 2). The locus coeruleus (LC), characterized by its high degree and eigenvector centrality, as well as its notably higher betweenness centrality, underscores its pivotal role in propagating and integrating neural signals within the ISO-influenced network. In the KET group, the temporal association areas (TEa) serve as a hub, emphasizing their integrative function in the manifestation of ketamine-induced dissociative anesthesia. Meanwhile, the PAG and the lateral septal nucleus, rostral part (LSr), function as central hubs in the home cage and saline groups, respectively.

Discussion

In this study, a comparative analysis was conducted on the effects of two general anesthetics, ISO and KET, on c-Fos expression throughout the brain. Hierarchical cluster analysis enabled a detailed examination of individual brain region responses to each anesthetic. We found that KET primarily activates the cerebral cortex, indicative of a top-down mechanism, whereas ISO chiefly stimulates subcortical areas, particularly the hypothalamus, aligning with a bottom-up approach (***Mashour, 2014***; ***Mashour and Hudetz, 2017***). Further analysis based on c-Fos expression revealed the TEa as a key hub in the KET-induced network and the LC in the ISO network, underscoring their significant roles in mediating the effects of KET and ISO, respectively.

Our hierarchical clustering method effectively identified brain regions impacted by ISO and KET, aligning with multiple comparison results as shown in Figures 4 and 5. This approach facilitated the efficient grouping of regions with similar expression patterns, enabling a comprehensive analysis of brain-wide c-Fos expression differences. Notably, certain brain regions such as SO, VLPO, TU, and CeA were prominent under ISO treatment, with SO (***Jiang-Xie et al., 2019***), VLPO (***Moore et al., 2012***), and CeA (***Hua et al., 2020***) previously reported to be involved in mechanisms of general anesthesia. The LC was identified as a highly connected hub, underscoring its critical role in the brainstem during ISO-induced general anesthesia. The LC is known for its diverse functions, including arousal, pain modulation, attention, stress response, and neuroprotection. Studies indicate that chemical activation of the LC enhances whole-brain functional connectivity, largely due to its role as the primary source of norepinephrine (NE) and its extensive influence throughout the brain (***Zerbi et al., 2019***). The significant activation of the LC and its pivotal position in the functional network underlying ISO-induced unconsciousness indicate its crucial role in maintaining and integrating the network. This finding highlights the LC's involvement in the bottom-up paradigm of ISO-induced unconsciousness.

KET induces extensive activation across the brain, with a notable impact on cortical and cerebral nuclei, as indicated in Figures 3 and 4. This observation aligns with the proposal by Mashour et al. that anesthesia-induced unconsciousness includes both the modulation of bottom-up and top-down neural processing (***Mashour, 2014***; ***Mashour and Hudetz, 2017***). In this framework, anesthetics like KET diminish consciousness by interfering with cortical and thalamocortical circuits, which are crucial for neural information integration. Our study found that KET administration significantly activates cortical and subcortical arousal-promoting nuclei. Graph theoretical analysis

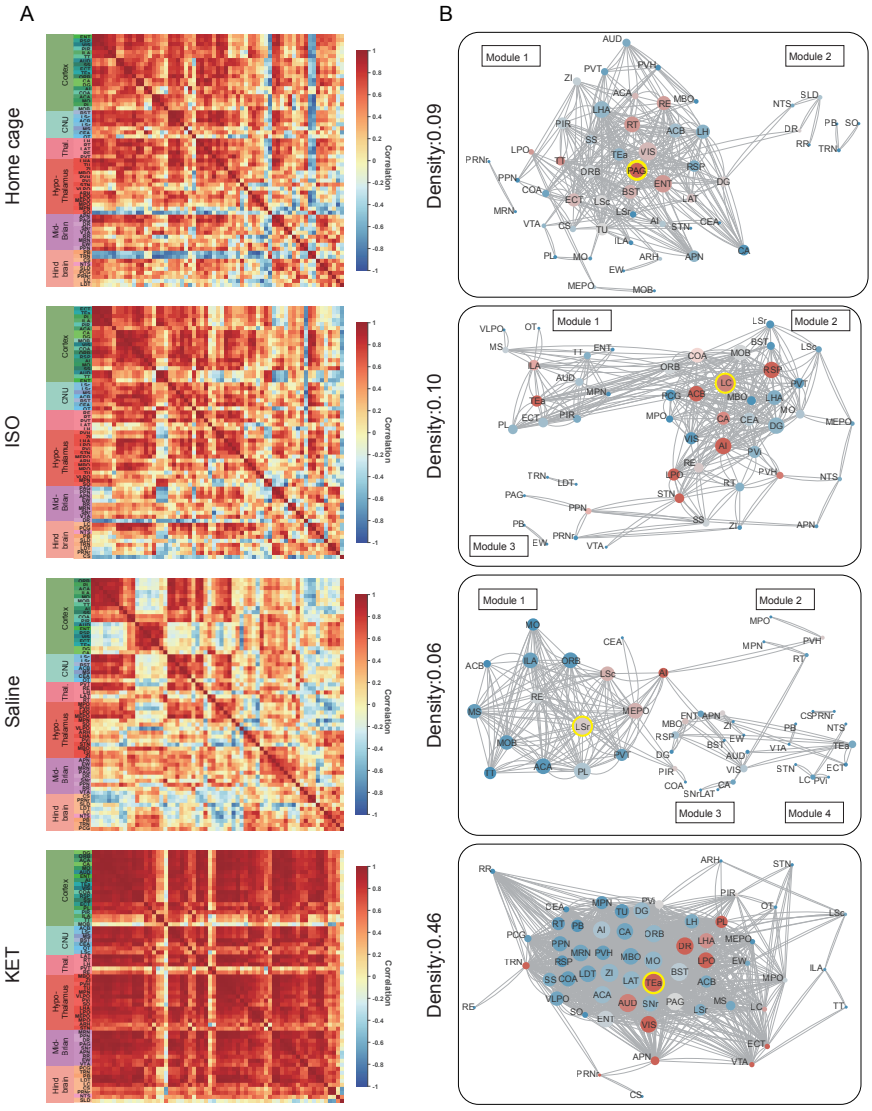

Figure 6. Generation of anesthetics-induced networks and identification of hub regions. (A) Heatmaps display the correlations of log c-Fos densities within brain regions (CTX, CNU, TH, HY, MB, and HB) for various states (home cage, ISO, saline, KET). Correlations are color-coded according to Pearson's coefficients. The brain regions within each anatomical category are organized by hierarchical clustering of their correlation coefficients. Full names and expression levels for each brain region are detailed in Supplementary Figure 3. (B) Network diagrams illustrate significant positive correlations ($P < 0.05$) between regions, with Pearson's r exceeding 0.82. Edge thickness indicates correlation magnitude, and node size reflects the number of connections (degree). Node color denotes betweenness centrality, with a spectrum ranging from dark blue (lowest) to dark red (highest). The networks are organized into modules consistent with the clustering depicted in Figure 6—figure supplement 1A.

Figure 6—figure supplement 1. Hierarchical clustering across different conditions. (A) Heatmaps depict the hierarchical clustering of brain regions within the home cage, ISO, saline, and KET groups, using Euclidean distance matrices calculated from correlation coefficients. Each brain region is represented by its abbreviation, with full names and expression levels detailed in Figure 3—figure supplement 1. Modules are demarcated within each dendrogram at a cut-off threshold of 0.7. (B) Silhouette scores are plotted against the dendrogram tree height ratio for each condition, with optimal cluster definition indicated by a dashed line at a 0.7 ratio. (C) The number of clusters formed at different cutoff levels. At a ratio of 0.7, ISO and saline treatments result in three clusters, whereas home cage and KET conditions yield two clusters. (D) The mean Pearson's correlation coefficient (r) was computed from interregional correlations displayed in Figure 6A. Data were analyzed using one-way ANOVA with Tukey's post hoc test, ***$P < 0.001$.

Figure 6—figure supplement 2. Hub region characterization across different conditions: home cage (A), ISO (B), saline (C), and KET (D) treatments. Brain regions are sorted by degree, betweenness centrality, and eigenvector centrality, with each metric presented in separate bar graphs. Bars to the left of the dashed line indicate the top 20% of regions by rank, highlighting the most central nodes within the network. Red bars signify regions that consistently appear within the top rankings for both degree and betweenness centrality across the metrics.

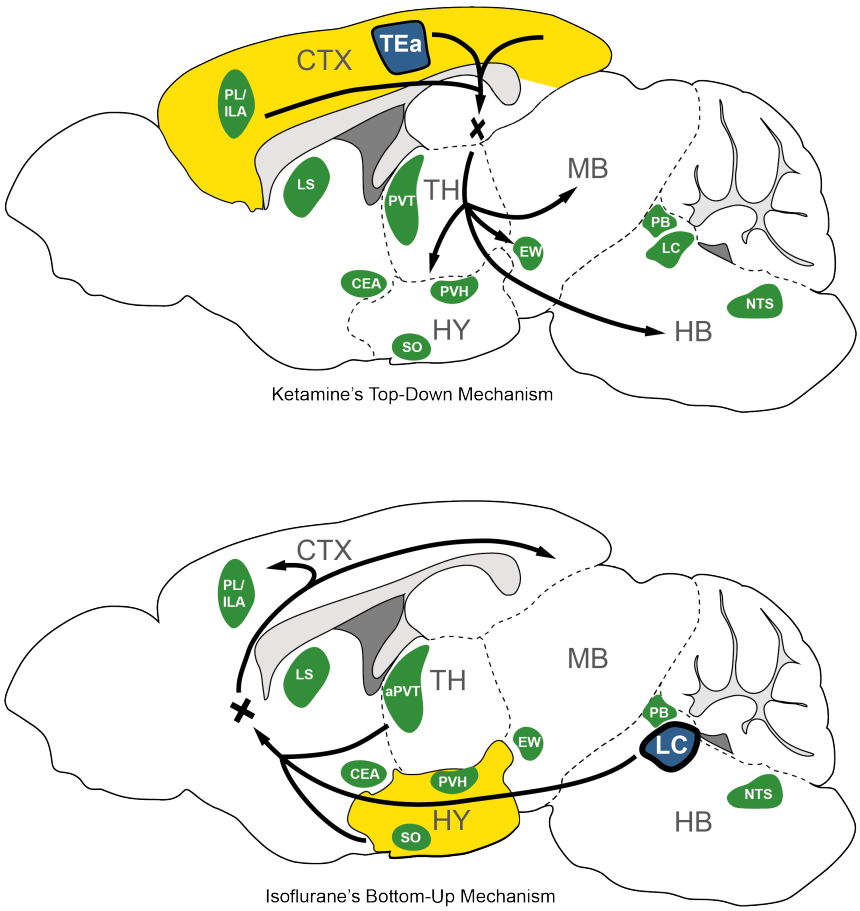

Figure 7. The possible framework for KET and ISO-induced unconsciousness. The distinct pathways of KET and ISO-induced unconsciousness can be explained by two contrasting mechanisms. The 'top-down' process attributes KET's effect to widespread cortical activation (represented in yellow), with the temporal association areas (TEa) acting as the central node in the functional network (depicted in blue). Conversely, the 'bottom-up' approach suggests that isoflurane-induced unconsciousness stems from the activation of certain hypothalamic regions (highlighted in yellow), with the locus coeruleus (LC) acting as the hub node within the isoflurane-induced functional network. Nuclei activated by both anesthetics are shown in green. Adapted from (***Mashour, 2014***; ***Mashour and Hudetz, 2017***; ***Reimann and Niendorf, 2020***). PL, prelimbic area; ILA, infralimbic areas; SO, supraoptic nucleus; PVH, paraventricular hypothalamic nucleus; LC, locus coeruleus; SS, somatosensory cortex; CTX: cortex; TH: thalamus; HY, hypothalamus; MB; midbrain; HB, hindbrain.

identified the TEa as a central hub in the KET-induced functional network. Given TEa's critical role in integrating multisensory information, particularly auditory signals, and its involvement in complex behaviors such as maternal responses as evidenced by its role in processing pup ultrasonic vocalizations, our findings suggest that KET may influence the connectivity of TEa with other brain regions, thus potentially altering the overall dynamics of the functional brain network (***Tasaka et al., 2020***). This further supports the significance of cortical areas during KET anesthesia.

Identifying shared neural features between KET and ISO is crucial for understanding anesthetic-induced unconsciousness. The coactivation of brain regions, such as PL/ILA and aPVT, alongside analgesia-related nuclei like CeA, PB, and LC, suggests a shared mechanism for thalamocortical regulation and common pathways for pain relief. This observation provides valuable insights into the fundamental mechanisms of anesthesia-induced hypnosis and analgesia. Additionally, the coactivation of neuroendocrine-related nuclei, particularly PVH and SO in the hypothalamus, raises questions about the potential influence of anesthetics on hormonal release and homeostatic regulation. Further investigation is warranted for other coactivated nuclei, such as EW and NTS, to understand their roles in anesthesia. The coactivated nuclei suggest a potential shared neuronal circuitry for general anesthesia, encompassing common features like unconsciousness, analgesia, and autonomic regulation. Future research could focus on examining coactivated brain regions by the two anesthetics or manipulating identified hub nodes to delve deeper into the mechanisms of general anesthesia.

Our findings indicate that c-Fos expression in the KET group is significantly elevated compared to the ISO group, and the saline group exhibits notably higher c-Fos expression than the home cage group, as seen in Figure 3—figure supplement 1. Intraperitoneal saline injections in the saline group, despite pre-experiment acclimation with handling and injections for four days, may still evoke pain and stress responses in mice. Subtle yet measurable variations in brain states between the home cage and saline groups were observed, characterized by changes in normalized EEG delta/theta power (home cage: 0.05±0.09; saline: -0.03±0.11) and EMG power (home cage: -0.37±0.34; saline: 0.04±0.13), as shown in Figure 1—figure supplement 1. These changes suggest a relative increase in overall brain activity in the saline group compared to the home cage group, potentially contributing to the higher c-Fos expression. Although the difference in EEG power between the ISO group and the home cage control was not significant, the increase in EEG power observed in the ISO group was similar to that of KET (0.47 ± 0.07 vs 0.59 ± 0.10), suggesting that both agents may induce loss of consciousness in mice. Regarding EMG power, ISO showed a significant decrease in EMG power compared to its control group. In contrast, the KET group showed a lesser reduction in EMG power (ISO: -1.815± 0.10; KET: -0.96 ± 0.21), which may partly explain the higher overall c-Fos expression levels in the KET group. This is consistent with previous studies where ketamine doses up to 150 mg/kg increase delta power while eliciting a wakefulness-like pattern of c-Fos expression across the brain (***Lu et al., 2008***). Furthermore, the observed differences in c-Fos expression may arise in part from the dosages, routes of administration, and their distinct pharmacokinetic profiles. This variation is compounded by the lack of detailed physiological monitoring, such as blood pressure, heart rate, and respiration, affecting our ability to precisely assess anesthesia depth. Future studies incorporating comprehensive physiological monitoring and controlled dosing regimens are essential to further elucidate these relationships and refine our understanding of the effects of anesthetics on brain activity.

Methods and Materials

Animals

All animal experiments were conducted in accordance with the National Institutes of Health guidelines and were approved by the Chinese Academy of Sciences' Institute of Neuroscience. Adult male wild-type (WT) mice (C57BL/6J) (8-10 weeks old, weight from 22 to 26 g) were purchased from institute-approved vendors (LingChang Experiment Animal Co., China). Mice were individ-

ually housed and maintained on a 12 h:12 h light/dark cycle (lights on at 07:00 a.m. and off at 07:00 p.m.) with food and water available ad libitum.

Drug administration

All experiments were conducted between 13:00-14:30 (ZT6–ZT7.5). We adapted mice to handling and the anesthesia chamber (10×15×15 cm) for four days to minimize experimental confound-induced c-Fos induction. For KET administration, adult male mice were handled for 10 minutes per day, and normal saline (NS) was injected intraperitoneally (i.p.) for four consecutive days at 13:00. On day five, a randomly chosen mouse received an injection of ketamine (Gutian Medicine, H35020148) (n=6), and the control groups (n=8) received the same volume of saline. ISO group (n=6) mice were handled and inhaled 1.5% isoflurane (RWD Life Science, 1903715) at 13:00 on day four in the chamber. Meanwhile, the control groups (n=6) were left undisturbed in their home cages prior to sampling. We confirmed the loss of righting reflex at 5 min after anesthetics exposure. For 90 min after KET injection or ISO inhalation, mice were deeply anesthetized with 5% ISO and transcardially perfused with 35 ml 0.1 M phosphate-buffered saline (PBS) followed by 35 ml 4% paraformaldehyde (PFA). The brains were then removed and postfixed overnight with 4% PFA. Following fixation, the brains were dehydrated for 48 hours with 30% sucrose (wt/vol) in PBS. Coronal sections (50 μm) of the whole brain were cut using a cryostat (HM525 NX, Thermo Scientific) after being embedded with OCT compound (NEG-50, Thermo Scientific) and freezing.

Anesthesia depth measurement

EEG and EMG recordings were conducted as previously described (***Luo et al., 2023***). Specifically, a stainless steel electrode was positioned over the frontal cortex for EEG measurements, while an insulated EMG electrode was inserted into the neck muscles. Additionally, a reference electrode was placed above the cerebellum. The EEG/EMG data were captured using TDT system-3 amplifiers, specifically RZ5 + RA16PA and RZ2 + PZ5 configurations. To measure the depth of anesthesia using EEG/EMG signals, a fast Fourier transform spectral analysis was employed, featuring a frequency resolution of 0.18 Hz. Data was noted every 5 seconds through a MATLAB tool and subsequently verified manually by experts. The assessment was based on EMG power and the ratio of EEG's δ power (0.5-4Hz) to θ power (6-10Hz). EEG and EMG power values within 30 minutes post-administration were normalized to a 5-minute pre-administration baseline.

Immunohistochemistry

One out of every three brain slices (100 μm intervals) of each whole brain was washed three times with 0.1 M phosphate-buffered saline (PBS) for 10 min and permeabilized for 30 minutes at room temperature with 0.3% Triton X-100 in PBS (PBST). Slices were incubated for 2 hours at room temperature with 2% normal donkey serum (Sigma, G6767) in PBS overnight at 4°C with c-Fos primary antibodies (226003, Synaptic Systems; 1:500) diluted in PBS with 1% donkey serum. After three washes with PBST, slices were incubated with the Cy3 donkey anti-rabbit (711165152, Jackson; 1:200) secondary antibody for 2 hours at room temperature. Immunostained slices were mounted with VECTASHIELD mounting medium with DAPI and then scanned under a fluorescent microscope equipped with a 10× objective (VS120, Olympus) or a confocal microscope with a 20× objective (FV300, Olympus). Due to the limited scope of a single field of view, either 2 or 4 adjacent fields of view were stitched together to offer a comprehensive representation of specific brain regions, including the PL, ILA, LSc, LSr, SS, and VISC.

Quantification of c-Fos positive cells

The procedures used for c-Fos analysis were based on previous research (***Ma et al., 2021***). A custom-written software package was employed for cellular quantification within brain images. The software consists of three components: atlas rotation, image registration, and signal detection.

Atlas rotation module

Utilizing the Allen Mouse Brain Atlas, this module allows rotations in both horizontal and vertical dimensions to align with mouse brain samples. To determine the appropriate rotation angles, we manually pinpointed anatomical landmarks corresponding to the samples. For the left-right axis rotation, we chose points from the CA3 pyramidal layer in both hemispheres and the posterior slice of the dentate gyrus, specifically the granule cell layer. For the dorsal-ventral axis rotation, we identified key anatomical landmarks. These include the initial connections of the anterior commissure and corpus callosum between the hemispheres, as well as ventral regions like the interpeduncular nucleus and the suprachiasmatic nucleus. After determining these rotation angles, we adjusted the reference atlas to match our samples.

Image registration module

This module uses a tool that aligns brain slice images with a reference atlas, facilitating the alignment of overall brain region distribution. Registration starts by matching the coronal plane of the sample sections to the atlas. After defining the external boundaries of the brain section, the system performs geometric transformations on the section to optimize its fit with the atlas.

Signal detection module

The detection module is designed to automatically label c-Fos+ cells. Post detection, a manual verification was performed on each digitized brain section image to ensure the accuracy and precision of the c-Fos+ cell markings.

Hierarchical clustering

Prior to hierarchical clustering in Figures 2 and 3, we calculated the relative c-Fos densities by dividing the c-Fos densities of each brain region in the experimental groups by their respective controls and then performed a log transformation on these values to obtain the log relative c-Fos densities. These log ratios, which normalize the data and reduce variance, indicate differential expression with a value of zero denoting no change compared to control. After normalizing the data, we performed hierarchical clustering by first computing the pairwise Euclidean distances among brain regions. Regions with the smallest distances, indicating high similarity, were grouped iteratively. Cluster boundaries were defined using complete linkage, ensuring homogeneity within clusters by considering the largest distance between members. In Figure 6, hierarchical clustering was performed within each of the CTX, CNU, TH, HY, MB, and HB regions based on the log-transformed c-Fos density correlations. In Figure 6—figure supplement 1, hierarchical clustering was performed based on the interregional log c-Fos density correlations to identify modules of coactivation within each treatment group, revealing underlying functional connectivity networks (***Kimbrough et al., 2020***). To determine the statistical significance of c-Fos expression differences, we computed the Z-score for each treatment condition—ISO and KET—by dividing the log relative c-Fos density by the standard error. Positive z-scores indicate higher values than control, and negative z-scores indicate lower values than control.

Network generation

To evaluate how functional connectivity changed under general anesthetics in WT mice, we extracted 63 brain regions from major brain subdivisions (cerebral cortex, cerebral nuclei, thalamus, hypothalamus, midbrain, and hindbrain) listed in Figure 6A. Correlation matrices were generated by computing Pearson correlation coefficients from interregional c-Fos expression in the 63 regions. Mean correlations were calculated to assess changes in functional connectivity between these major subdivisions of the brain. Weighted undirected networks were constructed by considering correlations with Pearson's $r \geq 0.82$, corresponding to a one-tailed significance level of $P<0.05$ (uncorrected). The nodes in the networks represent brain regions, and the correlations that survived thresholding were considered connections. Theoretical graph analysis was performed using

Brain Connectivity Toolbox (https://sites.google.com/site/bctnet/, version 2019-03-03) in MATLAB R2021 (The MathWorks Inc.) (***Rubinov and Sporns, 2010***). Network visualization was performed using Cytoscape (version 3.2.1) (***Shannon et al., 2003***).

Hub identification

Network centrality was evaluated using degree, betweenness, and eigenvector centrality measures to identify potential hub regions (***Guimera and Nunes Amaral, 2005***). Degree counts the number of edges connected to a node, signifying its immediate influence. Betweenness centrality is gauged by the number of shortest paths passing through a node, indicating its role as a connector or 'bridge' within the network. Eigenvector centrality measures a node's influence by the centrality of its connections, valuing nodes linked to well-connected neighbors. High eigenvector centrality indicates significant influence through these high-quality connections within the network.

Statistical analysis

Sample size was determined based on prior studies (***Lu et al., 2008***; ***Yatziv et al., 2020***). Data are presented as mean ± SEM. In Figures 4 and 5, independent t-tests evaluating differences in c-Fos expression for KET and ISO treatments were corrected for multiple comparisons using the Benjamini, Krieger, and Yekutieli method, with a 5% false discovery rate (Q) (***Benjamini and Hochberg, 1995***). Pearson correlation coefficients (R) were transformed into Z-scores using Fisher's Z transformation before computing group means and making statistical comparisons in Figure 6—figure supplement 1D. All statistical analyses were conducted using GraphPad Prism 9.0 (GraphPad Software, USA) and MATLAB R2021 (Mathworks Inc.).

Acknowledgments

We express our gratitude to our interns, Chuhang Wong from Imperial College London and Jiale Huang from ShanghaiTech University, for their assistance in cell counting.

Funding

This study was funded by the National Natural Science Foundation of China (grants 82271292, 81730031 to Yingwei Wang; 82371286, 82101350 to Mengqiang Luo), the Shanghai Municipal Key Clinical Specialty (grant shslczdzk06901 to Yingwei Wang), and the Foundation of Shanghai Municipal Science and Technology Medical Innovation Research Project (23Y21900600 to Yingwei Wang).

Author contributions

Yue Hu, Conceptualization, Formal analysis, Investigation, Visualization, Methodology, Writing—original draft, Writing—review and editing; Jiangtao Qi, Conceptualization, Software, Formal analysis; Zhao Zhang, Resources, Investigation, Supervision, Writing—review and editing; Mengqiang Luo, Resources, Supervision, Funding acquisition, Project administration, Writing—review and editing; Yingwei Wang, Conceptualization, Resources, Supervision, Funding acquisition, Project administration, Writing—review and editing.

Competing Interest Statement

All authors declare no competing financial interest.

References

Bekkers JM, Suzuki N. Neurons and circuits for odor processing in the piriform cortex. Trends Neurosci. 2013; 36(7):429–38. https://www.ncbi.nlm.nih.gov/pubmed/23648377, doi: 10.1016/j.tins.2013.04.005.

Benjamini Y, Hochberg Y. Controlling the False Discovery Rate: A Practical and Powerful Approach to Multiple Testing. Journal of the Royal Statistical Society Series B (Methodological). 1995; 57(1):289–300. http://www.jstor.org/stable/2346101.

Bliss TV, Collingridge GL, Kaang BK, Zhuo M. Synaptic plasticity in the anterior cingulate cortex in acute and chronic pain. Nat Rev Neurosci. 2016; 17(8):485–96. doi: 10.1038/nrn.2016.68.

Cheriyan J, Sheets PL. Altered Excitability and Local Connectivity of mPFC-PAG Neurons in a Mouse Model of Neuropathic Pain. J Neurosci. 2018; 38(20):4829–4839. doi: 10.1523/jneurosci.2731-17.2018.

Cho JR, Treweek JB, Robinson JE, Xiao C, Bremner LR, Greenbaum A, Gradinaru V. Dorsal Raphe Dopamine Neurons Modulate Arousal and Promote Wakefulness by Salient Stimuli. Neuron. 2017; 94(6):1205–1219.e8. doi: 10.1016/j.neuron.2017.05.020.

Deng J, Zhou H, Lin JK, Shen ZX, Chen WZ, Wang LH, Li Q, Mu D, Wei YC, Xu XH, Sun YG. The Parabrachial Nucleus Directly Channels Spinal Nociceptive Signals to the Intralaminar Thalamic Nuclei, but Not the Amygdala. Neuron. 2020; 107(5):909–923 e6. https://www.ncbi.nlm.nih.gov/pubmed/32649865, doi: 10.1016/j.neuron.2020.06.017.

Do JP, Xu M, Lee SH, Chang WC, Zhang S, Chung S, Yung TJ, Fan JL, Miyamichi K, Luo L, Dan Y. Cell type-specific long-range connections of basal forebrain circuit. Elife. 2016; 5. https://www.ncbi.nlm.nih.gov/pubmed/27642784, doi: 10.7554/eLife.13214.

Duncan GE, Moy SS, Knapp DJ, Mueller RA, Breese GR. Metabolic mapping of the rat brain after subanesthetic doses of ketamine: potential relevance to schizophrenia. Brain Res. 1998; 787(2):181–90. https://www.ncbi.nlm.nih.gov/pubmed/9518601, doi: 10.1016/s0006-8993(97)01390-5.

Feng H, Wen SY, Qiao QC, Pang YJ, Wang SY, Li HY, Cai J, Zhang KX, Chen J, Hu ZA, Luo FL, Wang GZ, Yang N, Zhang J. Orexin signaling modulates synchronized excitation in the sublaterodorsal tegmental nucleus to stabilize REM sleep. Nat Commun. 2020; 11(1):3661. doi: 10.1038/s41467-020-17401-3.

Franks NP. General anaesthesia: from molecular targets to neuronal pathways of sleep and arousal. Nat Rev Neurosci. 2008; 9(5):370–86. https://www.nature.com/articles/nrn2372.pdf, doi: 10.1038/nrn2372.

Gao C, Leng Y, Ma J, Rooke V, Rodriguez-Gonzalez S, Ramakrishnan C, Deisseroth K, Penzo MA. Two genetically, anatomically and functionally distinct cell types segregate across anteroposterior axis of paraventricular thalamus. Nat Neurosci. 2020; 23(2):217–228. https://www.ncbi.nlm.nih.gov/pubmed/31932767, doi: 10.1038/s41593-019-0572-3.

Gelegen C, Miracca G, Ran MZ, Harding EC, Ye Z, Yu X, Tossell K, Houston CM, Yustos R, Hawkins ED, Vyssotski AL, Dong HL, Wisden W, Franks NP. Excitatory Pathways from the Lateral Habenula Enable Propofol-Induced Sedation. Curr Biol. 2018; 28(4):580–587.e5. doi: 10.1016/j.cub.2017.12.050.

Guimera R, Nunes Amaral LA. Functional cartography of complex metabolic networks. Nature. 2005; 433(7028):895–900. https://www.ncbi.nlm.nih.gov/pubmed/15729348, doi: 10.1038/nature03288.

Gupta RG, Schafer C, Ramaroson Y, Sciullo MG, Horn CC. Role of the abdominal vagus and hindbrain in inhalational anesthesia-induced vomiting. Auton Neurosci. 2017; 202:114–121. https://www.ncbi.nlm.nih.gov/pubmed/27396693, doi: 10.1016/j.autneu.2016.06.007.

Han B, McCarren HS, O'Neill D, Kelz MB. Distinctive recruitment of endogenous sleep-promoting neurons by volatile anesthetics and a nonimmobilizer. Anesthesiology. 2014; 121(5):999–1009. doi: 10.1097/aln.0000000000000383.

Hase T, Hashimoto T, Saito H, Uchida Y, Kato R, Tsuruga K, Takita K, Morimoto Y. Isoflurane induces c-Fos expression in the area postrema of the rat. J Anesth. 2019; 33(4):562–566. doi: 10.1007/s00540-019-02662-0.

Hauer BE, Pagliardini S, Dickson CT. Prefrontal-Hippocampal Pathways Through the Nucleus Reuniens Are Functionally Biased by Brain State. Front Neuroanat. 2021; 15:804872. https://www.ncbi.nlm.nih.gov/pmc/articles/PMC8842257/pdf/fnana-15-804872.pdf, doi: 10.3389/fnana.2021.804872.

Hemmings J H C, Riegelhaupt PM, Kelz MB, Solt K, Eckenhoff RG, Orser BA, Goldstein PA. Towards a Comprehensive Understanding of Anesthetic Mechanisms of Action: A Decade of Discovery. Trends Pharmacol Sci. 2019; 40(7):464–481. doi: 10.1016/j.tips.2019.05.001.

Hua T, Chen B, Lu D, Sakurai K, Zhao S, Han BX, Kim J, Yin L, Chen Y, Lu J, Wang F. General anesthetics activate a potent central pain-suppression circuit in the amygdala. Nat Neurosci. 2020; 23(7):854–868. https://www.nature.com/articles/s41593-020-0632-8.pdf, doi: 10.1038/s41593-020-0632-8.

Inta D, Trusel M, Riva MA, Sprengel R, Gass P. Differential c-Fos induction by different NMDA receptor antagonists with antidepressant efficacy: potential clinical implications. Int J Neuropsychopharmacol. 2009; 12(8):1133–6. https://www.ncbi.nlm.nih.gov/pubmed/19638253, doi: 10.1017/S1461145709990319.

Jiang-Xie LF, Yin L, Zhao S, Prevosto V, Han BX, Dzirasa K, Wang F. A Common Neuroendocrine Substrate for Diverse General Anesthetics and Sleep. Neuron. 2019; 102(5):1053–1065.e4. doi: 10.1016/j.neuron.2019.03.033.

Kimbrough A, Lurie DJ, Collazo A, Kreifeldt M, Sidhu H, Macedo GC, D'Esposito M, Contet C, George O. Brain-wide functional architecture remodeling by alcohol dependence and abstinence. Proc Natl Acad Sci U S A. 2020; 117(4):2149–2159. https://www.ncbi.nlm.nih.gov/pubmed/31937658, doi: 10.1073/pnas.1909915117.

Lee U, Ku S, Noh G, Baek S, Choi B, Mashour GA. Disruption of frontal-parietal communication by ketamine, propofol, and sevoflurane. Anesthesiology. 2013; 118(6):1264–75. https://www.ncbi.nlm.nih.gov/pubmed/23695090, doi: 10.1097/ALN.0b013e31829103f5.

Leung LS, Luo T, Ma J, Herrick I. Brain areas that influence general anesthesia. Prog Neurobiol. 2014; 122:24–44. https://pdf.sciencedirectassets.com/271063/1-s2.0-S0301008214X00109/1-s2.0-S0301008214000896/main.pdf?X-Amz-Security-Token=IQoJb3JpZ2luX2VjECsaCXVzLWVhc3QtMSJHMEUCIA52tn%2F9KHIPV6z3jPJM2FjdyTTJWDjw0fTii1hFBp%2FVAiEAk6B1wk7bCw94kKnaEJAvmA6dI48nrDaJYh9ygy9SbKwqvQMI1%2F%2F%2F%2F%2F%2F%2F%2F%2F%2FARADGgwwNTkwMDM1NDY4NjUiDPWtIUb5DP6oqKbTriqRA3Gu7kPGQ1C2BJ2VkPiP3niDVtEvCiSIOkLwGobdhUVvtGY8AaMUUtJ%2FQg1Cuhgus1V1MrdG20UdqJJWbrAZkqJtZWBcEZdlXv6P0d2FM11qkLos9ETdhzO8wT05sQG7JEQOil%2Bsx7HC7PwEoSPAe8zynr96OuS%2BHlPw7ENXMx5McUByAj3%2FBjpE%2BUa49qJ0bI2u2VSIqdKiyeqycRFY9CfCKpGJmIIsxVQJ8ev9tyHfXv0QwoeysPBmY6Ec%2FHaQdFbMZHd%2BQ3s70z69jf64xdjuG8P8P5JBDP0iGFKSiUqHxjI%2F2ElLNiNv%2BAefqZlGVxYvpVUEAEqLapn6b1eeeVOa4rotvZUOx6Ov44lnPSU%2B19A99DC56iGVw0CRf8AL4f643HWOGOLe5ctcAcl2BIyE6Gd7r7oE9wefCO%2FGr%2BRpNNa0Z4HiR9tsXhfOZGRVBR2b1JfIONvJUgO3tHjWwbzbo6qvMLf5xfgFOusBnqvn2%2BKEJasSQCdUsoIQkOKlRnfOFW3Y%2FiiFmoXu%2FqwbZ93aorpR3WENOvYq1AFMOR24aGu2rLsE%2F4O2CofQc1OEkqY%2BzMgy1d3HES9TJcmb%2B5Op08rBwXLhPovxroDEXrJKAVc8NGg566q3SqzhLTEflnIAC4tvftcu92Bw2Peoab43OptWGFHiHbmY0Mau3qc1cHGU6SbBTcFJPkI%2BqnXq8DdXuXA25vBFdcDUl0rvQHfJl4OxDmvb4qbr%2B2BITxAPiuADZg%3D%3D&X-Amz-Algorithm=AWS4-HMAC-SHA256&X-Amz-Date=20200717T111429Z&X-Amz-SignedHeaders=host&X-Amz-Expires=300&X-Amz-Credential=ASIAQ3PHCVTY3ICHP4FY%2F20200717%2Fus-east-1%2Fs3%2Faws4_request&X-Amz-Signature=a85cdefcc800c36c91300a5d69c55e94a41f52f973f723bab65097208140e83a&hash=e5784b35f921ea415268c8c2a6d55703ca268042c943591013ac2b2430a89b270f6af2c76d8dfd086a07176afe7c76c2c61&pii=S0301008214000896&tid=spdf-0eaa05f3-53a7-4f74-b242-86bee9ad543f&sid=c881d61487516346ce1b53b26f1cc872c88fgxrqa&type=client, doi: 10.1016/j.pneurobio.2014.08.001.

Llorca-Torralba M, Camarena-Delgado C, Suárez-Pereira I, Bravo L, Mariscal P, Garcia-Partida JA, López□Martín C, Wei H, Pertovaara A, Mico JA, Berrocoso E. Pain and depression comorbidity causes asymmetric plasticity in the locus coeruleus neurons. Brain. 2021; 145(1):154–167. https://doi.org/10.1093/brain/awab239, doi: 10.1093/brain/awab239.

Lu J, Nelson LE, Franks N, Maze M, Chamberlin NL, Saper CB. Role of endogenous sleep-wake and analgesic systems in anesthesia. J Comp Neurol. 2008; 508(4):648–62. https://onlinelibrary.wiley.com/doi/abs/10.1002/cne.21685, doi: 10.1002/cne.21685.

Luo M, Fei X, Liu X, Jin Z, Wang Y, Xu M. Divergent Neural Activity in the VLPO During Anesthesia and Sleep. Adv Sci (Weinh). 2023; 10(2):e2203395. https://www.ncbi.nlm.nih.gov/pubmed/36461756, doi: 10.1002/advs.202203395.

Ma G, Liu Y, Wang L, Xiao Z, Song K, Wang Y, Peng W, Liu X, Wang Z, Jin S. Hierarchy in sensory processing reflected by innervation balance on cortical interneurons. Science Advances. 2021; 7(20):eabf5676.

Ma S, Allocca G, Ong-Pålsson EK, Singleton CE, Hawkes D, McDougall SJ, Williams SJ, Bathgate RA, Gundlach AL. Nucleus incertus promotes cortical desynchronization and behavioral arousal. Brain Struct Funct. 2017; 222(1):515–537. doi: 10.1007/s00429-016-1230-0.

Mashour GA. Top-down mechanisms of anesthetic-induced unconsciousness. Front Syst Neurosci. 2014; 8:115. https://fjfsdata01prod.blob.core.windows.net/articles/files/97687/pubmed-zip/.versions/1/.package-entries/fnsys-08-00115/fnsys-08-00115.pdf?sv=2015-12-11&sr=b&sig=DQhXzk4GgU12ckemlquDAU7hP2bisbegP0NFL7%2BjkWQ%3D&se=2020-07-20T11%3A30%3A05Z&sp=r&rscd=attachment%3B%20filename%2A%3DUTF-8%27%27fnsys-08-00115.pdf, doi: 10.3389/fnsys.2014.00115.

578 **Mashour GA**, Hudetz AG. Bottom-Up and Top-Down Mechanisms of General Anesthetics Modulate Different
579 Dimensions of Consciousness. Front Neural Circuits. 2017; 11:44. https://www.ncbi.nlm.nih.gov/pubmed/
580 28676745, doi: 10.3389/fncir.2017.00044.

581 **Mashour GA**, Pal D, Brown EN. Prefrontal cortex as a key node in arousal circuitry. Trends Neurosci. 2022;
582 45(10):722–732. doi: 10.1016/j.tins.2022.07.002.

583 **Moore JT**, Chen J, Han B, Meng QC, Veasey SC, Beck SG, Kelz MB. Direct Activation of
584 Sleep-Promoting VLPO Neurons by Volatile Anesthetics Contributes to Anesthetic Hypno-
585 sis. Current Biology. 2012; 22(21):2008–2016. <GotoISI>://WOS:000311060200021https:
586 //pdf.sciencedirectassets.com/272099/1-s2.0-S0960982212X00216/1-s2.0-S096098221201007X/
587 main.pdf?X-Amz-Security-Token=IQoJb3JpZ2luX2VjEFoaCXVzLWVhc3QtMSJGMEQCIH8%
588 2BpugW51xKo2mrZciq9280hRSPcqQDuqOmv7gIb8m7AiBmprGF%2BzMdhmAlgG%2FZ0DU%2FV2%
589 2Bt8PoNeF8Q8695QD%2BleCq0AwhyEAMaDDA1OTAwMzU0Njg2NSIMY1EmPgKfdw9fUDC3KpEDPw6lrY%
590 2FvPUuFMQsnsIzM8w2Ppr2PsL1WITcyn3wbIAMJesKPjxP6x0Ubn9Mh2ZlO7c5CCRjq%
591 2FXu3eNOyuMa776VZnpDmjP2GtcqGZPf%2B9V2XDQsfpY9wH2PnQHWqPv2siWiQA%
592 2FupXtzjOCUj3zHem5tWEnYaZ5DT2Avkqif0xzjGNwo6jhyHxSUmKltcWt6oD2XELdabpDI7d9FKDO%
593 2Fe5vGOj89Q3B2bIzDrJ3%2BrUvP2vpi2HMfvctubSGIortJ%2FuWobHbRmvpiLiMWdNJ16enNMU2ID818ToXWn3qOg1Z
594 2FbEdxNWTWozXP14sFGgHMIKGvlU45Lzb4DaXFAS4BIHnd27ualdmI%2BFSUzczaQl0b%2FWIel8c9%
595 2BA604XRk6gj8tL2nQ9TX%2F2vqsWEatf0U09MVEgxdDZzYB80Z%2BVwowQtRGyGTZz9mXePUNO3VtWGGJB%
596 2F8M7djrR4NFP1eHCKSdfYQJ5l50mIkpD9rWA2dPd6WXXbJ5cYLWD2kwufzV9AU67AGD96RBz243J0Fpujf7kZdXSxIkn
597 2F0Y6WfVBnekUDMWDY3OSygoYAEzS%2FkCXrscCCIM7F4NGuxx9HVx%2B4A5aB%
598 2F1ejqKaTUQho4zKv4Zoyy3%2BxHweTVoEIMA%2BbvKxVR8h1x7ReMvGnyv2eetjKwDg287Vhapc32RcdwSrCV5965XiRc
599 2BenpbpXO6vVOPeiPqljzki5Sc46pXJeQBYv7BM1u5OG5JnwTV31ukz9PLLR5cqvNLpHSJSCYM57NtwVsEUjZ6r8SxnIhIe
600 3D%3D&X-Amz-Algorithm=AWS4-HMAC-SHA256&X-Amz-Date=20200414T101801Z&X-Amz-SignedHeaders=
601 host&X-Amz-Expires=300&X-Amz-Credential=ASIAQ3PHCVTYTZDG4E5R%2F20200414%2Fus-east-1%
602 2Fs3%2Faws4_request&X-Amz-Signature=f4fc003b5db61663368fd46e6927f48c77431cb39aee171b702c6799b9c2b6e3&has
603 dc8024703c2127ccad892535d338a447fbe124c93c201b14c0a92fa8bef4a57e&host=68042c943591013ac2b2430a89b270f6af2
604 S096098221201007X&tid=spdf-5fd88eb2-512b-40dd-b7c6-851b6f5ac7bc&sid=39c44ec174a86049570b455972a24819d705g
605 client, doi: 10.1016/j.cub.2012.08.042.

606 **Morgan JI**, Curran T. Stimulus-transcription coupling in neurons: role of cellular immediate-early genes. Trends
607 Neurosci. 1989; 12(11):459–62. doi: 10.1016/0166-2236(89)90096-9.

608 **Musacchio T**, Rebenstorff M, Fluri F, Brotchie JM, Volkmann J, Koprich JB, Ip CW. Subthalamic nucleus deep
609 brain stimulation is neuroprotective in the A53T α-synuclein Parkinson's disease rat model. Ann Neurol.
610 2017; 81(6):825–836. doi: 10.1002/ana.24947.

611 **Nagata A**, Nakao S, Miyamoto E, Inada T, Tooyama I, Kimura H, Shingu K. Propofol inhibits ketamine-induced
612 c-fos expression in the rat posterior cingulate cortex. Anesth Analg. 1998; 87(6):1416–20. https://www.ncbi.
613 nlm.nih.gov/pubmed/9842840, doi: 10.1097/00000539-199812000-00040.

614 **Nagata A**, Nakao Si S, Nishizawa N, Masuzawa M, Inada T, Murao K, Miyamoto E, Shingu K. Xenon inhibits but
615 N(2)O enhances ketamine-induced c-Fos expression in the rat posterior cingulate and retrosplenial cortices.
616 Anesth Analg. 2001; 92(2):362–8. doi: 10.1097/00000539-200102000-00016.

617 **Nakao S**, Arai T, Mori K, Yasuhara O, Tooyama I, Kimura H. High-dose ketamine does not induce c-Fos protein
618 expression in rat hippocampus. Neurosci Lett. 1993; 151(1):33–6. doi: 10.1016/0304-3940(93)90038-m.

619 **Nakao S**, Miyamoto E, Masuzawa M, Kambara T, Shingu K. Ketamine-induced c-Fos expression in the mouse
620 posterior cingulate and retrosplenial cortices is mediated not only via NMDA receptors but also via sigma
621 receptors. Brain Res. 2002; 926(1-2):191–6. doi: 10.1016/s0006-8993(01)03338-8.

622 **Nelson LE**, Guo TZ, Lu J, Saper CB, Franks NP, Maze M. The sedative component of anesthesia is mediated by
623 GABA(A) receptors in an endogenous sleep pathway. Nat Neurosci. 2002; 5(10):979–84. doi: 10.1038/nn913.

624 **Reimann HM**, Niendorf T. The (Un)Conscious Mouse as a Model for Human Brain Functions: Key Principles of
625 Anesthesia and Their Impact on Translational Neuroimaging. Front Syst Neurosci. 2020; 14:8. https://www.
626 ncbi.nlm.nih.gov/pubmed/32508601, doi: 10.3389/fnsys.2020.00008.

627 **Rubinov M**, Sporns O. Complex network measures of brain connectivity: uses and interpre-
628 tations. Neuroimage. 2010; 52(3):1059–69. https://www.ncbi.nlm.nih.gov/pubmed/19819337, doi:
629 10.1016/j.neuroimage.2009.10.003.

Schroeder KE, Irwin ZT, Gaidica M, Nicole Bentley J, Patil PG, Mashour GA, Chestek CA. Disruption of corticocortical information transfer during ketamine anesthesia in the primate brain. Neuroimage. 2016; 134:459–465. doi: 10.1016/j.neuroimage.2016.04.039.

Shannon P, Markiel A, Ozier O, Baliga NS, Wang JT, Ramage D, Amin N, Schwikowski B, Ideker T. Cytoscape: a software environment for integrated models of biomolecular interaction networks. Genome research. 2003; 13(11):2498–2504. https://pubmed.ncbi.nlm.nih.gov/14597658https://www.ncbi.nlm.nih.gov/pmc/articles/PMC403769/, doi: 10.1101/gr.1239303.

Smith ML, Li J, Cote DM, Ryabinin AE. Effects of isoflurane and ethanol administration on c-Fos immunoreactivity in mice. Neuroscience. 2016; 316:337–43. https://www.ncbi.nlm.nih.gov/pubmed/26742790, doi: 10.1016/j.neuroscience.2015.12.047.

Tasaka GI, Feigin L, Maor I, Groysman M, DeNardo LA, Schiavo JK, Froemke RC, Luo L, Mizrahi A. The Temporal Association Cortex Plays a Key Role in Auditory-Driven Maternal Plasticity. Neuron. 2020; 107(3):566–579 e7. https://www.ncbi.nlm.nih.gov/pubmed/32473095, doi: 10.1016/j.neuron.2020.05.004.

Villarreal CF, Del Bel EA, Prado WA. Involvement of the anterior pretectal nucleus in the control of persistent pain: a behavioral and c-Fos expression study in the rat. Pain. 2003; 103(1-2):163–74. https://www.ncbi.nlm.nih.gov/pubmed/12749971, doi: 10.1016/s0304-3959(02)00449-9.

Wheeler AL, Teixeira CM, Wang AH, Xiong X, Kovacevic N, Lerch JP, McIntosh AR, Parkinson J, Frankland PW. Identification of a functional connectome for long-term fear memory in mice. PLoS Comput Biol. 2013; 9(1):e1002853. https://www.ncbi.nlm.nih.gov/pubmed/23300432, doi: 10.1371/journal.pcbi.1002853.

Xu W, Wilson DA. Odor-evoked activity in the mouse lateral entorhinal cortex. Neuroscience. 2012; 223:12–20. https://www.sciencedirect.com/science/article/pii/S0306452212008159, doi: https://doi.org/10.1016/j.neuroscience.2012.07.067.

Yap EL, Greenberg ME. Activity-Regulated Transcription: Bridging the Gap between Neural Activity and Behavior. Neuron. 2018; 100(2):330–348. https://www.ncbi.nlm.nih.gov/pubmed/30359600, doi: 10.1016/j.neuron.2018.10.013.

Yatziv SL, Yudco O, Dickmann S, Devor M. Patterns of neural activity in the mouse brain: Wakefulness vs. General anesthesia. Neurosci Lett. 2020; 735:135212. https://www.ncbi.nlm.nih.gov/pubmed/32593772, doi: 10.1016/j.neulet.2020.135212.

Yeung JC, Yaksh TL, Rudy TA. Concurrent mapping of brain sites for sensitivity to the direct application of morphine and focal electrical stimulation in the production of antinociception in the rat. Pain. 1977; 4(1):23–40. https://www.ncbi.nlm.nih.gov/pubmed/927879, doi: 10.1016/0304-3959(77)90084-7.

Yi T, Wang N, Huang J, Wang Y, Ren S, Hu Y, Xia J, Liao Y, Li X, Luo F, Ouyang Q, Li Y, Zheng Z, Xiao Q, Ren R, Yao Z, Tang X, Wang Y, Chen X, He C, et al. A Sleep-Specific Midbrain Target for Sevoflurane Anesthesia. Adv Sci (Weinh). 2023; p. e2300189. https://www.ncbi.nlm.nih.gov/pubmed/36961096, doi: 10.1002/advs.202300189.

Zerbi V, Floriou-Servou A, Markicevic M, Vermeiren Y, Sturman O, Privitera M, von Ziegler L, Ferrari KD, Weber B, De Deyn PP, Wenderoth N, Bohacek J. Rapid Reconfiguration of the Functional Connectome after Chemogenetic Locus Coeruleus Activation. Neuron. 2019; 103(4):702–718 e5. https://www.ncbi.nlm.nih.gov/pubmed/31227310, doi: 10.1016/j.neuron.2019.05.034.

Zhang D, Liu J, Zhu T, Zhou C. Identifying c-fos Expression as a Strategy to Investigate the Actions of General Anesthetics on the Central Nervous System. Curr Neuropharmacol. 2022; 20(1):55–71. https://www.ncbi.nlm.nih.gov/pubmed/34503426, doi: 10.2174/1570159X19666210909150200.

Table 1. Figure 4—source data 1. Summary of prior studies on ketamine activated brain regions identified via c-Fos immunostaining.

Brain regions	Function	Treatment Regimen	Duration	Time of day	Effect	References
CeA	Pain Suppression	100mg/kg and 10mg/kgxylazine i.p.	2h	/	Up-regulated	Hua T, et al.,(2022) (***Hua et al., 2020***)
SO	Natural sleep/General anesthesia	100mg/kg with or without xylazine(10mg/kg) i.p.	2h	/	Up-regulated	Jiang-Xie LF, et al.,(2019) (***Jiang-Xie et al., 2019***)
pCC	/	100mg/kg i.p.	2h	/	Up-regulated	Nagata A, et al.,(1998) (***Nagata et al., 1998***)
pCC, RSC	/	100mg/kg i.p.	2h	/	Up-regulated	Nagata A, et al.,(2001) (***Nagata et al., 2001***)
RSP, CeA, Midline thalamic nuclei	Antidepressant	10mg/kg i.p.	1.5h	/	Up-regulated	Inta D, et al.,(2009) (***Inta et al., 2009***)
Cg, BF, Orx, TMN, vlPAG, LC, LHb, EW, midline thalamus	LC/vPAG engaged in analgesia	150mg/kg; 60mg/kg; 30mg/kg i.p.	2h	ZT3	Up-regulated	Lu J, et al.,(2008) (***Lu et al., 2008***)
CC, PVT	/	100mg/kg i.p.	/	/	/	Nakao S, et al.,(1993) (***Nakao et al., 1993***)
PC, RSP	/	50mg/kg i.p.	2h	ZT3-9	Up-regulated	Nakao S, et al.,(2002) (***Nakao et al., 2002***)

Table 2. Figure 5—source data 1. Summary of prior studies on brain regions activated by isoflurane, as detected through c-Fos immunostaining.

Brain regions	Function	Concentration of ISO	Duration	Time of day		References
VLPO	Sleep-Promoting, Hypnosis	1.2%, 0.6%, 0.3%	2h	ZT12-14/ZT4-6	Up-regulated	Moore JT,.et al.,(2012) (***Moore et al., 2012***)
PIR, LSD, LSV	/	4% 5mins+1%	2h	ZT2-7	Up-regulated	Smith ML, et al.,(2016) (***Smith et al., 2016***)
NTS, VeN	Vomiting	1% and 3%	1.5h	/	Up-regulated	Gupta RG, et al.,(2016) (***Gupta et al., 2017***)
CeA	Pain Suppression	1.5%	2h	/	Up-regulated	Hua T, et al.,(2022) (***Hua et al., 2020***)
SO	Natural sleep, General anesthesia	1%,1.2%	2h	/	Up-regulated	Jiang-Xie LF, et al.,(2019) (***Jiang-Xie et al., 2019***)
VLPO, MnPO	Sleep and unconsciousness	1.2%	2h	ZT14-17	Up-regulated	Han B, et al.,(2022) (***Han et al., 2014***)
EW, VLPO, LC	Sleep-Promoting, analgesia	2%	2h	ZT12	Up-regulated	Lu J, et al.,(2008) (***Lu et al., 2008***)
AP	Nausea, vomiting	1.3%,2.6%	2h	/	Up-regulated	Hase T, et al.,(2019) (***Hase et al., 2019***)

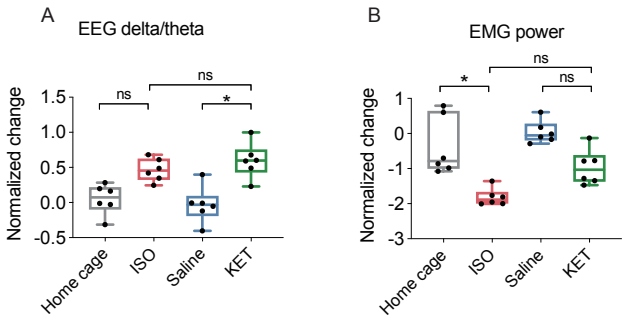

Figure 1—figure supplement 1. EEG and EMG power change after each treatment. The box represents the 25th-75th percentiles; the central line denotes the median; whiskers indicate maximum and minimum values. n = 6, 6, 8, 6 for the home cage, ISO, saline, and KET, respectively. (A) Normalized change in EEG power: ISO vs KET, P > 0.99; Saline vs KET, P = 0.01; Home cage vs ISO, P = 0.11. (B) Normalized change in EMG power: ISO vs KET, P = 0.36; Saline vs KET, P = 0.30; Home cage vs ISO, P = 0.02. Analyses were conducted using the Kruskal-Wallis test, followed by Dunn's multiple comparisons tests.

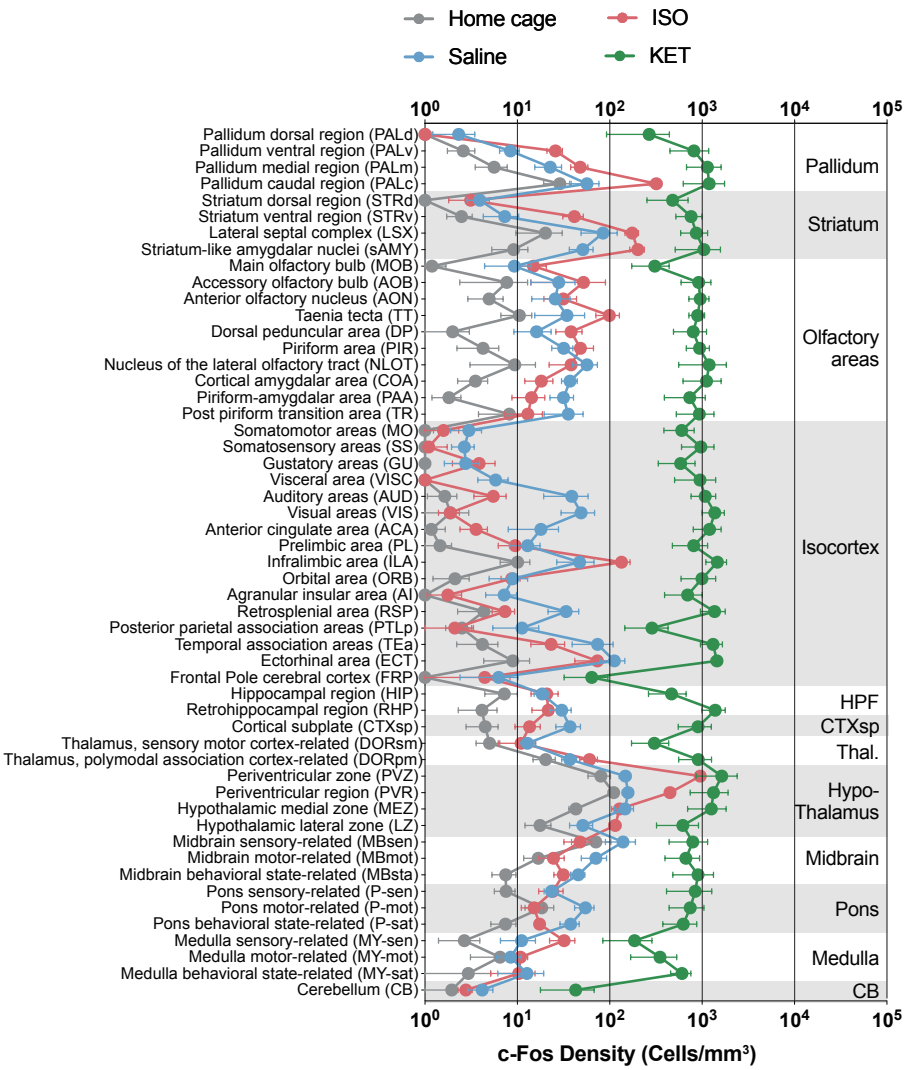

672

Figure 2—figure supplement 1. The c-Fos density in 53 brain areas for different conditions. (home cage, n = 6; ISO, n = 6 mice; saline, n = 8; KET, n = 6). Each point represents the c-Fos density in a specific brain region, denoted on the y-axis with both abbreviations and full names. Data are shown as mean ± SEM. Brain regions are categorized into 12 brain structures, as indicated on the right side of the graph.

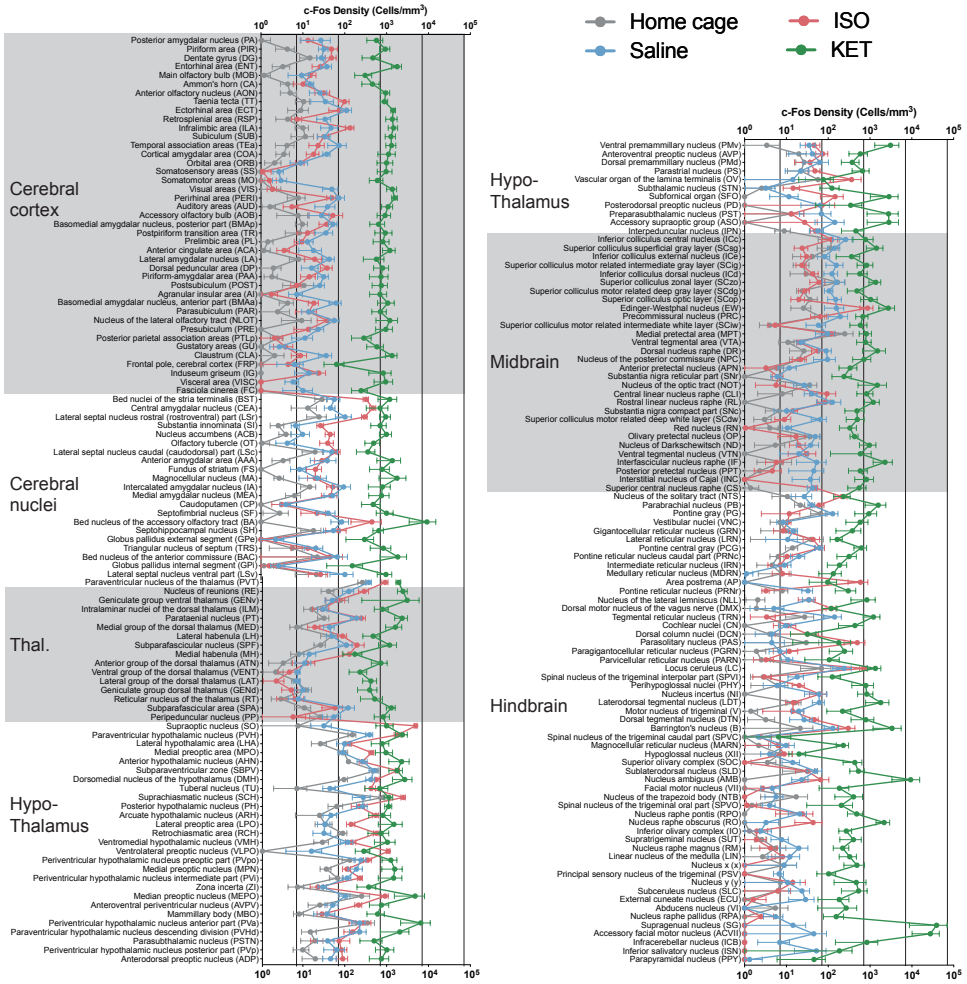

Figure 3—figure supplement 1. c-Fos density visualization across 201 distinct brain regions under various conditions. The graph depicts the c-Fos density levels for each condition, with data presented as mean and standard error. Brain regions with statistically significant differences are featured in Figures 4 and 5. Brain regions are organized into major anatomical subdivisions, as indicated on the left side of the graph.

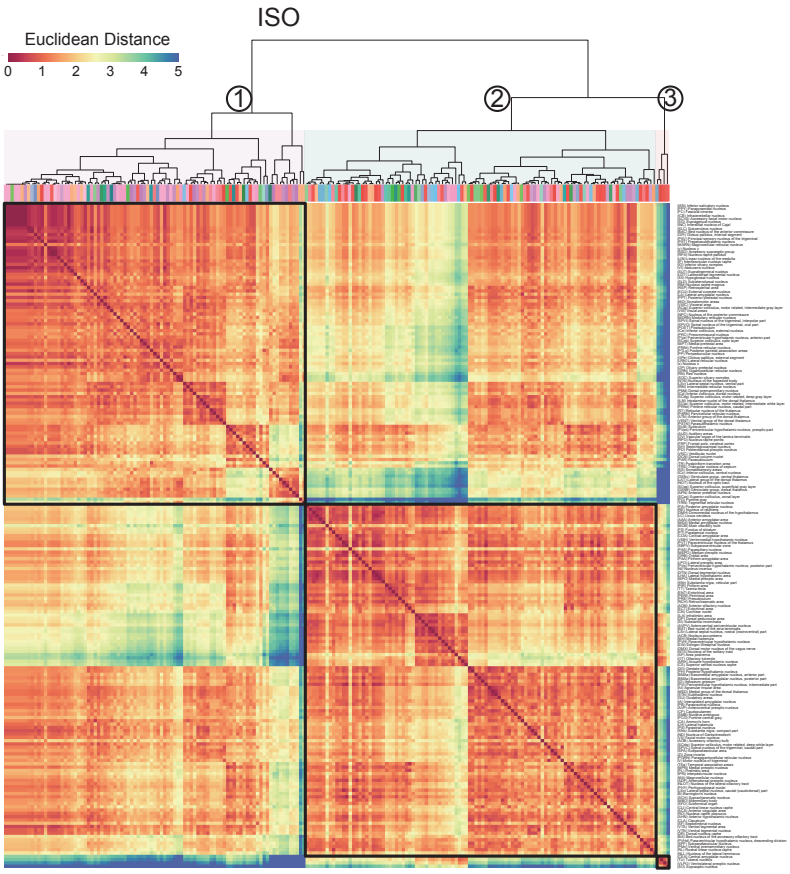

Figure 3—figure supplement 2. Region labels for the hierarchical clustering of the ISO group in Figure 3A.

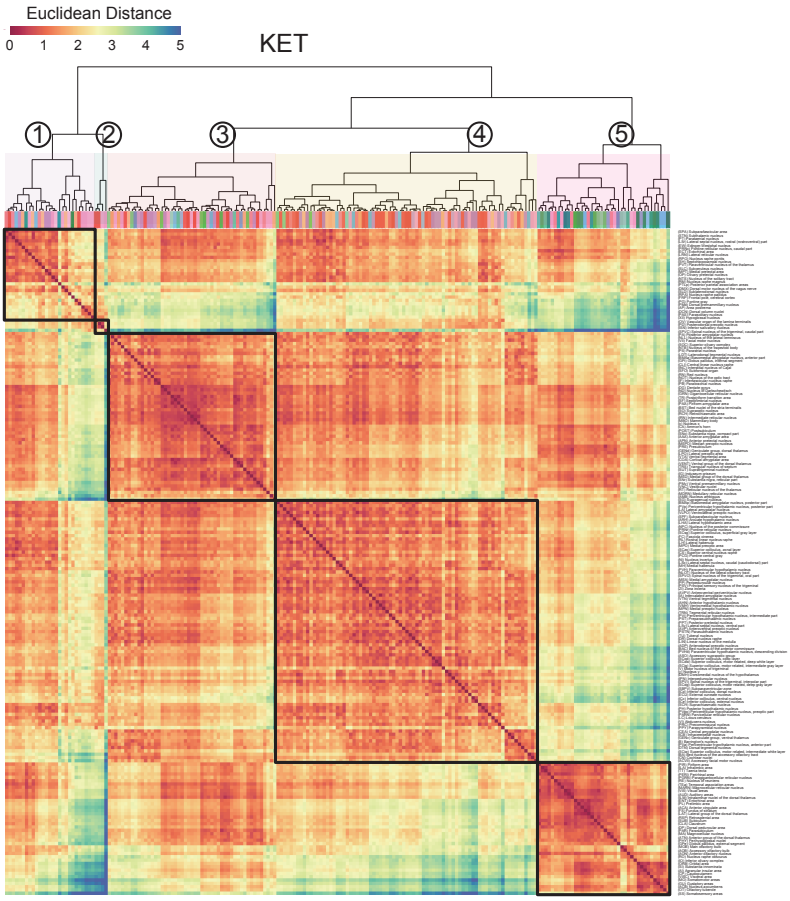

675

Figure 3—figure supplement 3. Region labels for the hierarchical clustering of the KET group in Figure 3A.

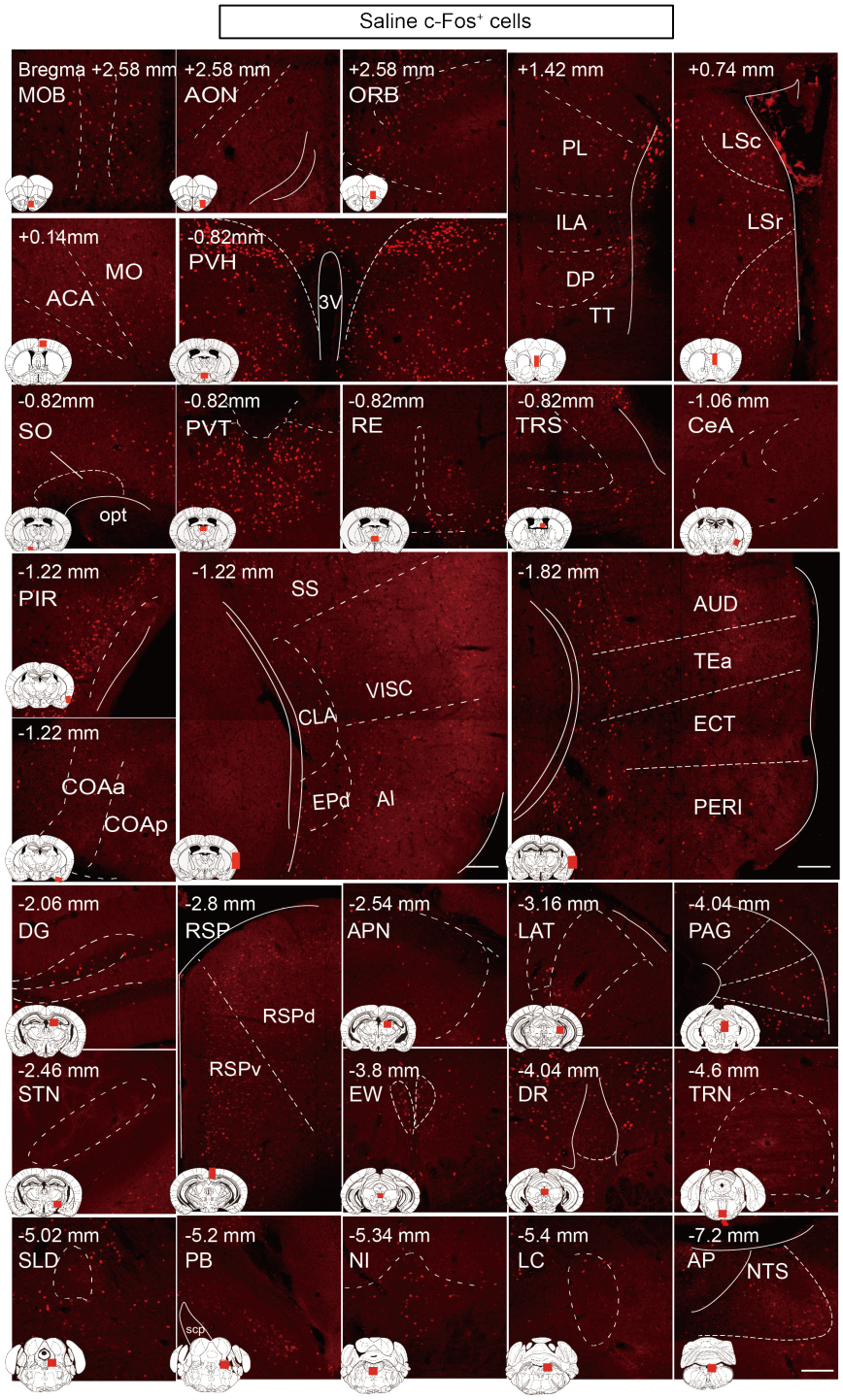

Figure 4—figure supplement 1. c-Fos expression in specific brain regions following normal saline administration. (A) Representative immunohistochemical staining of c-Fos+ cells in MOB, AON, ORB, MPO, ACA, MO, TRS, PL, ILA, DP, LS, PVT, SO, PVH, RE, VISC, AI, CLA, EPd, PIR, COA, AUD, TEa, ECT, PERI, CeA, SS, DG, STN, RSP, APN, LAT, EW, DR, PAG, SLD, PB, TRN, NI, LC, and NTS. Scale bar represents 200 μm.

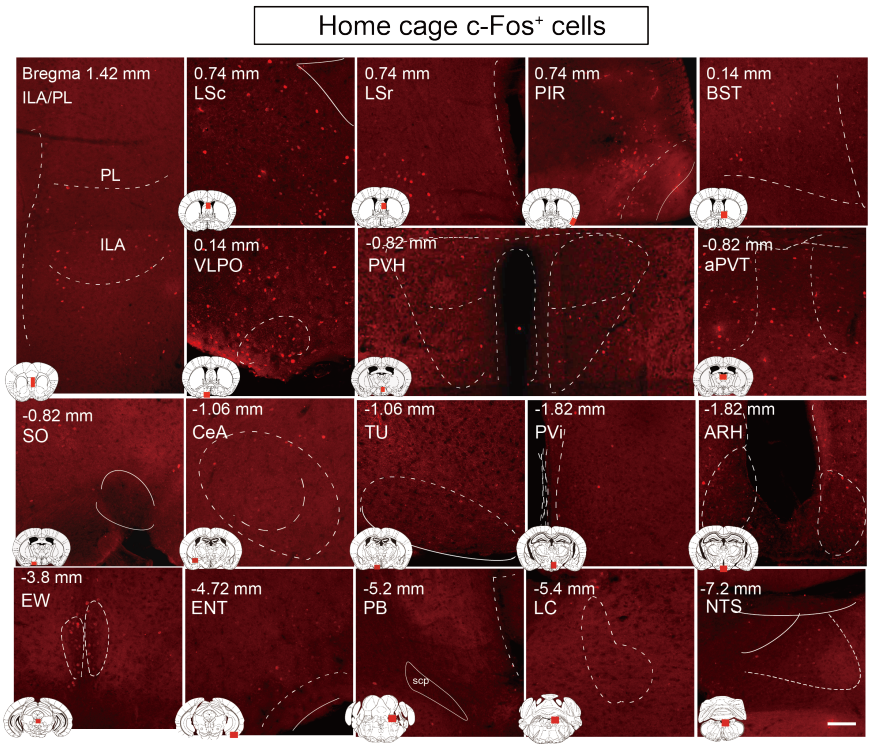

Figure 5—figure supplement 1. c-Fos expression in home cage group. (A) Representative immunohistochemical staining of c-Fos+ cells in PL, ILA, LSc, LSr, PIR, BST, VLPO, PVH, aPVT, SO, CeA, TU, PVi, ARH, EW, ENT, PB, LC, and NTS c-Fos+ cells from the indicated mice. Scale bar, 200 μm.

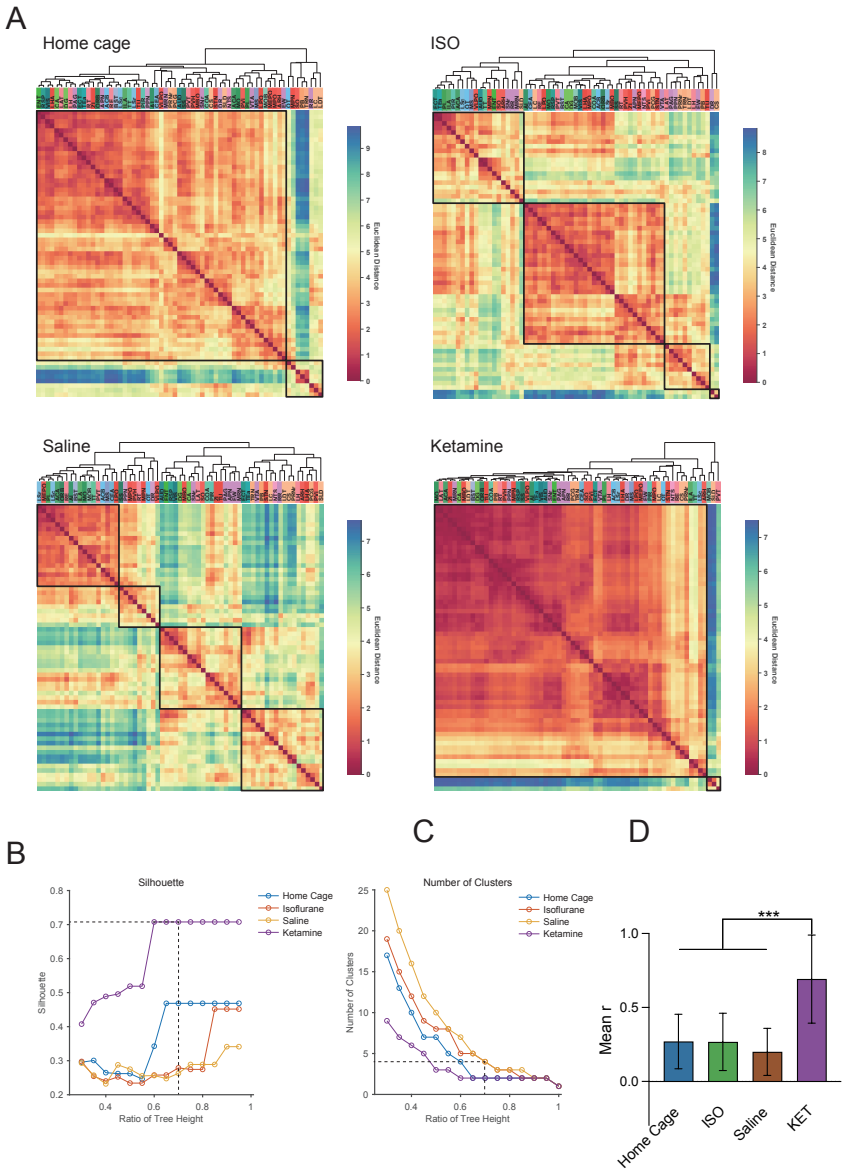

678

Figure 6—figure supplement 1. Hierarchical clustering across different conditions. (A) Heatmaps depict the hierarchical clustering of brain regions within the home cage, ISO, saline, and KET groups, using Euclidean distance matrices calculated from correlation coefficients. Each brain region is represented by its abbreviation, with full names and expression levels detailed in Figure 3—figure supplement 1. Modules are demarcated within each dendrogram at a cut-off threshold of 0.7. (B) Silhouette scores are plotted against the dendrogram tree height ratio for each condition, with optimal cluster definition indicated by a dashed line at a 0.7 ratio. (C) The number of clusters formed at different cutoff levels. At a ratio of 0.7, ISO and saline treatments result in three clusters, whereas home cage and KET conditions yield two clusters. (D) The mean Pearson's correlation coefficient (r) was computed from interregional correlations displayed in Figure 6A. Data were analyzed using one-way ANOVA with Tukey's post hoc test, ***P < 0.001.

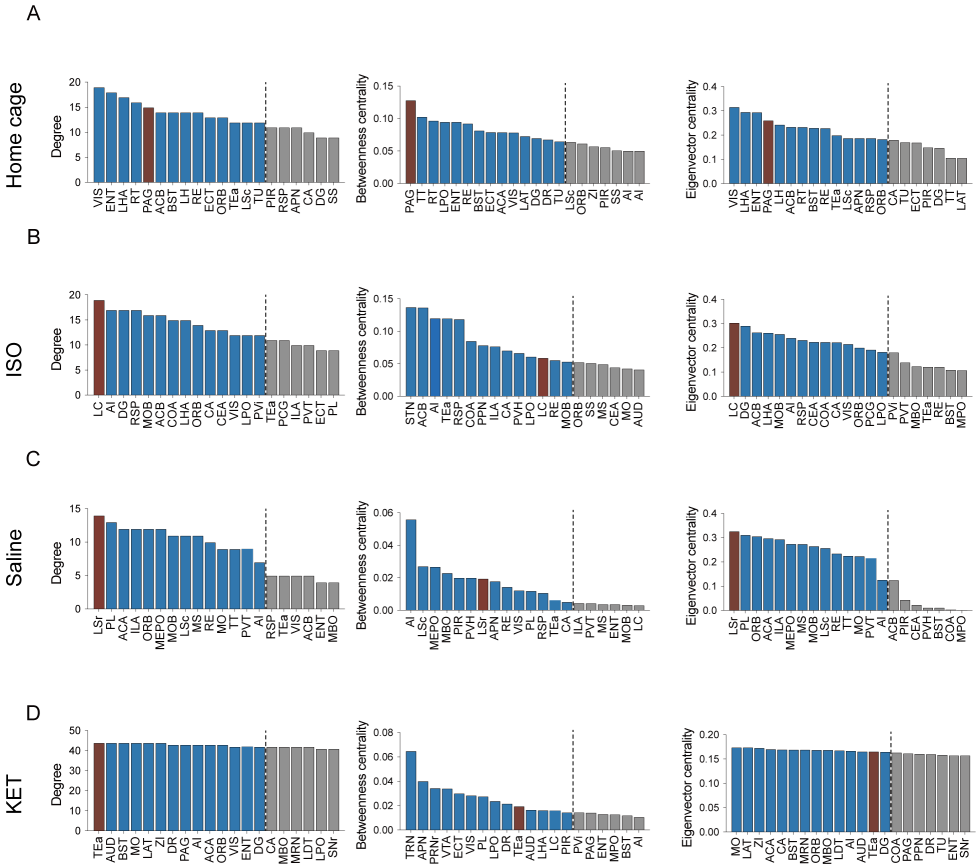

Figure 6—figure supplement 2. Hub region characterization across different conditions: home cage (A), ISO (B), saline (C), and KET (D) treatments. Brain regions are sorted by degree, betweenness centrality, and eigenvector centrality, with each metric presented in separate bar graphs. Bars to the left of the dashed line indicate the top 20% of regions by rank, highlighting the most central nodes within the network. Red bars signify regions that consistently appear within the top rankings for both degree and betweenness centrality across the metrics.